Atmos. Meas. Tech., 14, 1379–1403, 2021
https://doi.org/10.5194/amt-14-1379-2021

Atmospheric Measurement Techniques
Open Access
EGU

Comparison of co-located refractory black carbon (rBC) and elemental carbon (EC) mass concentration measurements during field campaigns at several European sites

Rosaria E. Pileci[1], Robin L. Modini[1], Michele Bertò[1], Jinfeng Yuan[1], Joel C. Corbin[1,a], Angela Marinoni[2], Bas Henzing[3], Marcel M. Moerman[3], Jean P. Putaud[4], Gerald Spindler[5], Birgit Wehner[5], Thomas Müller[5], Thomas Tuch[5], Arianna Trentini[6], Marco Zanatta[7], Urs Baltensperger[1], and Martin Gysel-Beer[1]

[1]Laboratory of Atmospheric Chemistry, Paul Scherrer Institute (PSI), 5232 Villigen, Switzerland
[2]Institute of Atmospheric Science and Climate, Italian National Research Council (CNR-ISAC), via Gobetti 101, 40129 Bologna, Italy
[3]Netherlands Organisation for Applied Scientific Research (TNO), 3584 Utrecht, the Netherlands
[4]Joint Research Centre (JRC), European Commission, 21027 Ispra, Italy
[5]Leibniz Institute for Tropospheric Research (TROPOS), 04318 Leipzig, Germany
[6]Regional Agency for Prevention, Environment and Energy, Emilia–Romagna, 40122, Bologna, Italy
[7]Alfred Wegener Institute, Helmholtz Centre for Polar and Marine Research, 27515 Bremerhaven, Germany
[a]now at: Metrology Research Centre, National Research Council Canada, Ottawa K1A 0R6, Canada

Correspondence: Robin L. Modini (robin.modini@psi.ch) and Martin Gysel-Beer (martin.gysel@psi.ch)

Received: 14 May 2020 – Discussion started: 25 June 2020
Revised: 4 January 2021 – Accepted: 7 January 2021 – Published: 23 February 2021

Abstract. The mass concentration of black carbon (BC) particles in the atmosphere has traditionally been quantified with two methods: as elemental carbon (EC) concentrations measured by thermal–optical analysis and as equivalent black carbon (eBC) concentrations when BC mass is derived from particle light absorption coefficient measurements. Over the last decade, ambient measurements of refractory black carbon (rBC) mass concentrations based on laser-induced incandescence (LII) have become more common, mostly due to the development of the Single Particle Soot Photometer (SP2) instrument. In this work, EC and rBC mass concentration measurements from field campaigns across several background European sites (Palaiseau, Bologna, Cabauw and Melpitz) have been collated and examined to identify the similarities and differences between BC mass concentrations measured by the two techniques. All EC concentration measurements in $PM_{2.5}$ were performed with the EUSAAR-2 thermal–optical protocol. All rBC concentration measurements were performed with SP2 instruments calibrated with the same calibration material as recommended in the literature. The observed values of median rBC-to-EC mass concentration ratios on the single-campaign level were 0.53, 0.65, 0.97, 1.20 and 1.29, respectively, and the geometric standard deviation (GSD) was 1.5 when considering all data points from all five campaigns. This shows that substantial systematic bias between these two quantities occurred during some campaigns, which also contributes to the large overall GSD. Despite considerable variability in BC properties and sources across the whole dataset, it was not possible to clearly assign reasons for discrepancies to one or the other method, both known to have their own specific limitations and uncertainties. However, differences in the particle size range covered by these two methods were identified as one likely reason for discrepancies.

Overall, the observed correlation between rBC and EC mass reveals a linear relationship with a constant ratio, thus providing clear evidence that both methods essentially quantify the same property of atmospheric aerosols, whereas systematic differences in measured absolute values by up to a factor of 2 can occur. This finding for the level of agreement between two current state-of-the-art techniques has important implications for studies based on BC mass concentra-

tion measurements, for example for the interpretation of uncertainties in inferred BC mass absorption coefficient values, which are required for modeling the radiative forcing of BC. Homogeneity between BC mass determination techniques is also very important for moving towards a routine BC mass measurement for air quality regulations.

1 Introduction

Light-absorbing aerosols exert a positive radiative forcing through direct absorption of solar radiation. Moreover, their heating can change atmospheric dynamics and, thereby, cloud formation and lifetime (Samset et al., 2018). Despite the relatively small mass abundance of black carbon (8 %–17 %; Putaud et al., 2010), it dominates the aerosol light absorption in the atmosphere (Bond et al., 2013). Additional, significant contributions come from brown carbon (Kirchstetter et al., 2004), tar balls (Adachi et al., 2019) and mineral dust (Sokolik and Toon, 1999).

Black carbon aerosols possess a unique set of properties: they are refractory (Schwarz et al., 2006), strong absorbers of short- and long-wave radiation (Bond and Bergstrom, 2006), insoluble in water (Fung, 1990), and composed primarily of graphene-like sp^2-bonded carbon (Medalia and Heckman, 1969). The source of black carbon is the incomplete combustion of hydrocarbon fuels, including fossil fuels and bio-fuels (Bond et al., 2013). BC mass concentration data from atmospheric measurements are used in many applications such as validation of model simulations (Grahame et al., 2014; Hodnebrog et al., 2014) and quantification of the mass absorption coefficient of BC (MAC_{BC}). The latter is defined as the ratio of the light absorption coefficient caused by BC to the BC mass concentration and is a crucial parameter in modeling the BC radiative forcing (Matsui et al., 2018). For these reasons, it is important to assess the accuracy and comparability of different BC mass measurement techniques.

There is neither an SI (International System of Units) traceable reference method nor a suitable standard reference material for quantifying BC mass (Baumgardner et al., 2012; Petzold et al., 2013). This presents a challenge for the long-term, routine monitoring of BC mass concentrations in observation networks such as GAW (Global Atmosphere Watch), ACTRIS (Aerosol, Clouds and Trace Gases Research Infrastructure) and IMPROVE (Interagency Monitoring of Protected Visual Environments). The lack of a reference method is due to variability in the microstructure of BC produced by different combustion sources (Adachi et al., 2010), the difficulty of isolating BC from other particulate matter and the lack of direct mass-based methods selective with respect to BC without interferences (Baumgardner et al., 2012).

In practice, the BC mass is defined operationally through methodologies that use distinct physico-chemical and/or optical properties of BC in order to quantify its mass concentration in aerosols. The following three different techniques are most commonly applied: filter based thermal–optical evolved gas analysis (Huntzicker et al., 1982; Chow et al., 2007; Cavalli et al., 2010); laser-induced incandescence (LII) (Schraml et al., 2000; Stephens et al., 2003; Schwarz et al., 2006; Michelsen et al., 2015) and methods based on aerosol light absorption (Rosen et al., 1978; Hansen et al., 1984; Arnott et al., 2003; Petzold et al., 2005). The specific terms used to refer to the mass of BC quantified by each of these three techniques are as follows: elemental carbon (EC), refractory black carbon (rBC) and equivalent black carbon (eBC), respectively (Petzold et al., 2013). Measurements of eBC mass are not further addressed here, as they rely on prior knowledge or assumed values of the MAC_{BC}. Such prior knowledge is not required for thermal–optical measurements of EC mass or for LII measurements of rBC mass.

Both thermal–optical analysis (TOA) and the LII technique make use of the high refractoriness of BC to quantify its mass, although in different manners. In comparing these two techniques, it is essential to define what is meant by BC. The popular Bond et al. (2013) definition of BC is, fundamentally, a summary of the properties of highly graphitized carbon found in soot particles. There are, however, other forms of light-absorbing carbonaceous particulate matter (PM), with different cross sensitivities for TOA and LII. Building on earlier studies (e.g., Bond, 2001), Corbin et al. (2019) recently proposed a refined classification of light-absorbing carbonaceous PM into four classes: soot–BC, char BC, tar brown carbon and soluble brown carbon, and they provided an overview of the respective physico-chemical properties. This refined classification provides a useful framework in describing the responses of TOA and LII. For example tar brown carbon, an amorphous form of carbon, is sufficiently refractory to contribute to EC mass, whereas it is not sufficiently refractory to cause substantial interference in rBC (Corbin and Gysel-Beer, 2019). Any work that compares BC measurement techniques should therefore consider the types of carbonaceous material present in the sample.

Very few intercomparisons of EC mass and rBC mass are available in the literature, particularly when it comes to ambient aerosols, despite the fact that both methods are frequently applied these days. This means that the debate on the comparability of these two quantities is still largely unresolved. Some studies have shown that the two quantities can agree to within a few percent (Laborde et al., 2012b; Miyakawa et al., 2016; Corbin et al., 2019), while other studies have shown they can systematically differ by factors of up to 2 to 3 in either direction (e.g., Zhang et al., 2016; Sharma et al., 2017).

In this work, we examined and quantified the level of agreement or disagreement between BC mass concentrations measured by thermal–optical analysis and the LII technique. For this purpose, we compared co-located measurements of EC and rBC mass concentrations from field campaigns performed at several European sites (Bologna,

Cabauw, Palaiseau and Melpitz) in order to sample different aerosol types. Care was taken to harmonize the applied methods: all thermal–optical measurements were performed with the same temperature protocol (EUSAAR-2, European Supersites for Atmospheric Aerosol Research; Cavalli et al., 2010), and all Single Particle Soot Photometer (SP2) calibrations were performed using the same calibration material. This first multi-site intercomparison allows us to more quantitatively assess the extent to which the EC and rBC concentration measurements agree or disagree with each other. Potential reasons for discrepancies such as different size cuts, calibration uncertainties and various interferences are discussed.

2 Methods

2.1 Sampling campaigns – measurements sites and experimental setup

The observations presented here include measurements from five field campaigns at four different sites, three of which are part of the ACTRIS network (Aerosol, Clouds and Trace Gases Research Infrastructure; https://www.actris.eu, last access: 16 February 2021). Basic information (site and country, station code, coordinates, altitude, year and season) of each field campaign is summarized in Table S1.

The Melpitz research site of TROPOS (Germany; 51°32′ N, 12°56′ E; 87 m a.s.l.) is located in the lowlands of Saxony, 41 km NE of Leipzig, Germany. The nearest village with about 230 inhabitants is 300 m east of the station. The site is representative of the regional background in central Europe (Spindler et al., 2012, 2013) since it is situated on a flat meadow, surrounded by agricultural land (Spindler et al., 2010). The area is sometimes influenced by long-range transported air masses from source regions in eastern, southeastern and southern Europe which can contain, especially in winter, emissions from coal heating (van Pinxteren et al., 2019). Two separate field campaigns were performed in summer (from 6 May to 1 July 2015) and winter (from 2 to 23 February 2017). During the two campaigns, the SP2 was placed behind a Nafion dryer (model MD-700, Perma Pure) with a PM_{10} inlet about 6 m above ground level (a.g.l.). The $PM_{2.5}$ sampler for the OC–EC samples was placed nearby. The meteorological conditions and aerosol characteristics encountered during the campaigns are described by Altstädter et al. (2018) for the summer campaign and by Yuan et al. (2021) for the winter campaign.

The KNMI (Koninklijk Nederlands Meteorologisch Instituut) Cabauw Experimental Site for Atmospheric Research (the Netherlands; 51°58′ N, 4°55′ E; 0.7 m a.s.l.) is located in the background area of Cabauw, 20 km from Utrecht, 30 km from Rotterdam and 50 km from the North Sea. The nearby region is agricultural in an otherwise densely populated area, and surface elevation changes are at most a few meters over 20 km. During the campaign, the SP2 was placed behind a Nafion dryer (model MD-700, Perma Pure) with a PM_{10} inlet situated at 4.5 m a.g.l. The PM_{10} sampler, from whose filters off-line OC–EC analyses were carried out, did not include a dryer in the sampling line in line with GAW recommendations (GAW Report No. 227; WMO, 2016). The measurements at this site were performed from 13 to 28 September 2016. The meteorological conditions and aerosol characteristics encountered during the campaign are described by Tirpitz et al. (2021).

The Bologna measurements were performed at the main seat of CNR-ISAC (Consiglio Nazionale delle Ricerche – Institute of Atmospheric Sciences and Climate), in Bologna (Italy; 44°31′ N, 11°20′ E; 39 m a.s.l.). The site is classified as urban background and is located in the Po Valley, a European pollution hot spot due to its orography, meteorological conditions and high presence of human activities, resulting in a large number of anthropogenic emission sources (Vecchi et al., 2009; Putaud et al., 2010; Ricciardelli et al., 2017; Bucci et al., 2018). During the campaign, a $PM_{2.5}$ sampler, not equipped with a drier, was situated at the ARPAE Supersito (inside the CNR-ISAC area). The SP2 was located inside a fully instrumented mobile van in the CNR parking area, about 50 m away from the ARPAE Supersito. The instruments in the van were connected to two inlet lines situated on the top of the vehicle at a height of 3 m and connected to the main inlet line with an inner diameter of 5 cm; no size cut was performed. The sampled air was dried to below 30 % relative humidity using two custom-built, silica-gel-loaded diffusion driers. The data presented in this paper were collected from 7 to 31 July 2017. The meteorological conditions and the aerosol properties of this campaign are described by Pileci et al. (2021).

The SIRTA Atmospheric Research Observatory (France; 48°43′ N, 2°12′ E; 160 m a.s.l.) is situated in Palaiseau, 25 km south of Paris. The station is characterized as suburban background (Haeffelin et al., 2005). This site is influenced by both fresh and aged black carbon mainly originating from the Paris area. It is impacted by road transport emissions all year round and residential wood burning during the winter (Laborde et al., 2013; Petit et al., 2015; Zhang et al., 2018). The SP2 along with many other instruments was installed in an air-conditioned trailer of the SIRTA measurement platform. For the OC–EC measurements, high-volume samplers with a $PM_{2.5}$ cut-off were available in the same area. The measurements were performed from 15 January to 15 February 2010. EC and rBC concentrations during this campaign have previously been published in Laborde et al. (2013).

2.2 Thermal–optical analysis

2.2.1 Measurement principle, OC–EC split and involved artifacts

In thermal–optical evolved gas analysis (TOA), carbonaceous particles deposited on a filter are thermally desorbed or reacted in order to determine the total carbon mass. This technique further divides the total carbon (TC) into EC and organic carbon (OC) according to the expectation that EC is refractory in an inert atmosphere while OC is not (Chow et al., 1993; Birch and Cary, 1996; Bond, 2001; Chow et al., 2004). Therefore, TOA provides operationally defined OC and EC mass rather than fundamental quantities. This basic binary split does not acknowledge that neither OC nor EC are well-defined materials. Instead, carbonaceous matter in aerosols populates the multidimensional space of chemical and physical properties more or less in a continuous manner (Saleh et al., 2018; Corbin et al., 2020). Nevertheless, the binary split approach aims at providing an operationally defined EC mass that corresponds to "true" BC mass as defined on a conceptual level by Bond et al. (2013) and Corbin et al. (2019) (see Sect. 1).

In TOA, the carbonaceous material deposited on a punch of a quartz fiber filter is thermally desorbed through progressive heating: first in an inert atmosphere of pure helium (He) at multiple moderate temperatures ($\sim$ 500–700 °C) (inert mode) and then in an oxidizing atmosphere (98 % He and 2 % O_2) at high temperature ($\sim$ 850 °C). The applied duration and the temperature of each step vary between different thermal protocols, as discussed below in Sect. 2.2.2. The evolving carbon is catalytically converted first to carbon dioxide (CO_2) and then to methane (CH_4). CH_4 is then quantified using a flame ionization detector (FID) and reported as OC (inert mode) and EC (oxidizing mode) mass. The instrument type applied in this study and most commonly used to perform TOA measurements is the OC–EC analyzer manufactured by Sunset Laboratory Inc. (Tigard, OR, USA).

Ideally, all OC would desorb in the inert He atmosphere and EC would exclusively burn off in the oxidizing O_2 atmosphere (Chow et al., 1993; Birch and Cary, 1996). In practice, a fraction of carbonaceous matter may be more refractory than the applied separation threshold while not being BC in a strict sense. This would cause a positive bias in measured EC mass. In addition, a fraction of the OC can pyrolyze in the He step to form pyrolytic carbon (PC), which is thermally stable and only desorbs in the O_2 step, thereby causing a charring artifact in the mutual quantification of OC and EC. To correct for this latter effect, a laser at 658 nm is used in combined thermal–optical analysis to monitor the light transmission through the loaded filter before and during the analysis. The measurement principle behind this so-called thermal–optical transmission (TOT) correction approach is explained in Sect. S1. The charring correction can also be performed using light reflectance (thermo-optical reflectance – TOR – method) instead of transmittance. As reported in the review paper by Karanasiou et al. (2015), EC values of atmospheric samples determined using the TOT method are often up to 30 %–70 % lower than those determined using the TOR method, which is attributed to various reasons (Karanasiou et al., 2015; Chiappini et al., 2014; see Sect. S1). Therefore, all EC mass values reported in this study are based on the TOT method.

The above-described assumptions about the optical charring correction are only partially fulfilled, typically leaving charring artifacts as a main source of bias even for optically corrected EC mass data (Chow et al., 2004; Subramanian et al., 2006). Pyrolysis depends on many factors, including the quantity and type of organic compounds, temperature steps in the analysis, and the residence time at each temperature step. This makes the TOA technique sensitive to the aerosol type collected on the filter. Water extraction experiments have shown that water-soluble organic carbon (WSOC) compounds are particularly prone to causing charring (Yu et al., 2002; Piazzalunga et al., 2011; Zhang et al., 2012; Giannoni et al., 2016). Samples with a high WSOC content come from, e.g., biomass and wood burning (Hitzenberger et al., 2006; Reisinger et al., 2008; Chen et al., 2015). A filter water-washing step prior to TOA can be used to remove WSOC, thereby reducing charring artifacts and improving comparability of different protocols for EC mass measurements (Yu et al., 2002; Piazzalunga et al., 2011). However, filter pre-washing is generally not applied in long-term-monitoring TOA measurements for practical reasons (the washing step is time-consuming). In these cases, the charring phenomenon can be reduced by adopting a thermal protocol with a sufficiently long residence time at each temperature step in the He atmosphere to allow for maximum OC evolution (Subramanian et al., 2006; Karanasiou et al., 2015).

The OC–EC split can be also biased by EC pre-combustion: EC can thermally evolve in the presence of oxidizing species (Watson et al., 2005; Corbin et al., 2014, 2015), and soluble inorganic compounds (Chow et al., 2001; Yu et al., 2002) and metal salts (Aakko-Saksa et al., 2018) can catalyze EC pre-combustion. If the amount of EC undergoing pre-combustion is significant relative to the amount of PC formed during the analysis, the optical correction (transmittance or reflectance) is not able to account for it, and this may cause an underestimation of the EC concentration.

Moreover, soluble brown carbon on filters can affect the laser correction if it was evolving during the OC steps, thereby causing a positive EC artifact. However, soluble brown carbon absorbs much less per unit mass than EC at the red wavelength ($\lambda = 635$ nm) of the laser used in the thermal–optical instruments, since its absorbance decreases strongly from the blue–UV region of the electromagnetic spectrum towards the red region (Karanasiou et al., 2015). This reduces the potential interference of soluble brown carbon via the introduction of a bias in the optical charring correction. Recently, Massabò et al. (2019) developed a modi-

fied Sunset Lab Inc. EC–OC analyzer to measure the brown carbon content in the sample by adding a second laser diode at $\lambda = 405$ nm.

Tar brown carbon only evolves in the oxidizing step of TOA due to its refractoriness (Corbin et al., 2019). Therefore, it is assigned to EC independent of its light absorption properties. This is in contrast to LII, where tar brown carbon only gives a marginal contribution to observed rBC mass (Sect. 2.3.3).

Further artifacts in TOA can be caused by carbonate carbon, as discussed in Wang et al. (2010), Karanasiou et al. (2015) and Querol et al. (2012). Thermal protocols can be designed to minimize this artifact by having most carbonate carbon evolve as OC (as is the case with the EUSAAR-2 protocol used in this work; Sect. 2.2.2). However, minor positive, carbonate-related artifacts in EC cannot be excluded (Karanasiou et al., 2011).

2.2.2 Thermal protocols – EUSAAR-2 vs. other existing protocols

Many variants of thermal protocols exist for the thermal–optical analysis of EC mass (Bautista et al., 2015). The results presented in this study are based on the EUSAAR-2 protocol, which was developed by Cavalli et al. (2010). The EUSAAR-2 protocol was specifically optimized for aerosol typically encountered at European background sites, and it has recently been selected as the European standard thermal protocol to be applied in air quality networks for the measurement of TC (total carbon), OC and EC in $PM_{2.5}$ (particulate matter) samples (European Committee for Standardization, 2017; EN 16909:2017). Besides EUSAAR-2, the IMPROVE–A thermal protocol of the Interagency Monitoring of Protected Visual Environments (Chow et al., 1993, 2007) and the NIOSH thermal protocols developed by the National Institute for Occupational Safety and Health (Birch and Cary, 1996) are also commonly used for TOA. Various NIOSH-like protocols (NIOSH 5040, NIOSH 840, NIOSH 850 and NIOSH 870) exist that are all modified versions of the Birch and Cary (1996) and Birch et al. (1999) protocols.

Table 1 summarizes the differences between EC measured with EUSAAR-2 and with other protocols reported in previous literature studies, with a particular focus on the thermal protocols that are considered in this study (e.g., see Fig. 6). The use of different thermal protocols can result in a wide elemental carbon-to-total-carbon variation by up to a factor of 5 (Cavalli et al., 2010). In general, it has been observed that protocols with a rather low peak temperature in the inert mode like EUSAAR-2 and IMPROVE generally classify more carbon as EC compared to the NIOSH protocol (Karanasiou et al., 2015). The EnCan-Total-900 protocol has a much longer retention time at each temperature step compared to the IMPROVE and NIOSH methods and does not involve a charring correction (Huang et al., 2006; Chan et al., 2010).

Table 1. Overview of reported differences between EC calculated with other protocols minus the EC calculated with the EUSAAR-2 protocol.

Protocols	Relative difference compared to EUSAAR-2 (TOT)
IMPROVE (TOR)	$\sim +25\,\%$[a]
IMPROVE–A (TOR)	$\sim -10\,\%$[b]
EnCan-Total-900	$\sim \pm 25\,\%$[c]

[a] Han et al. (2016). [b] Cheng et al. (2013). [c] Karanasiou et al. (2015).

2.2.3 Variability in EC measurements with the EUSAAR-2 protocol

Given the artifacts involved in TOA, different instruments can measure different EC concentrations for the same sample, even if the same thermal protocol is used. For this reason, the Joint Research Centre (JRC) European Reference Laboratory for Air Pollution (ERLAP) organizes annual instrumental inter-laboratory comparisons, which typically include 15 to 30 participants, in order to harmonize measurements from different Sunset instruments that employ the EUSAAR-2 protocol. The measurement performances are evaluated using several $PM_{2.5}$ quartz fiber filters collected at a regional background site in Italy. Since the true concentrations of EC or TC in these ambient samples are unknown (due to the lack of suitable reference methods or materials), the expected concentrations are chosen ("assigned") as the robust averages (i.e., with outliers removed) of the TC and EC mass concentrations measured by all participants.

The latest intercomparison yielded an EC-to-TC ratio repeatability (with the same instrument over time) of 3 % to 8 % and an EC-to-TC ratio reproducibility (among different instruments) of 12 % to 17 % (across 21 participants), where the method precision becomes exponentially poorer towards lower TC contents ($<10\,\mu g\,C\,cm^{-2}$) and lower EC-to-TC ratios (<0.07) (EMEP/CCC – Report 1/2018, https://projects.nilu.no/ccc/reports/cccr1_2018_Data_Report_2016_FINAL.pdf, last access: 16 February 2021). Table 2 presents EC bias and variability (see Sect. S2 of the Supplement for further information) for the instruments used in each campaign (based on data from the ERLAP intercomparison campaign that occurred most recently before or after the campaign in question). The Palaiseau campaign EC samples were analyzed by the Institute des Géosciences de l'Environnement (IGE, Grenoble); the Cabauw samples were analyzed by the Joint Research Centre (JRC, Italy); the Melpitz (summer and winter) samples were analyzed by the Leibniz-Institut für Troposphärenforschung (TROPOS); and the Bologna campaign samples

were analyzed by ARPAE. The EC bias and variability in the instrument used for analyzing the Bologna filter samples, which did not participate in a full ERLAP intercomparison, was determined by comparison with the JRC ERLAP reference instrument for nine filter samples from the Bologna campaign. The EC bias found was smaller than 20 % for all applied OC–EC analyzers, which is within the TOA measurement uncertainty. Therefore, we did not correct the EC measurements reported in this work for these biases.

Blank filters were analyzed for all campaigns. The blank value for EC mass was always below the detection limit or negligibly small compared to EC mass on loaded filter samples, such that applying a blank correction does not make a difference for the resulting EC mass concentration.

2.3 The Single Particle Soot Photometer (SP2)

2.3.1 Principle of measurement

Laser-induced incandescence occurs when a high-intensity laser is used to heat light-absorbing and highly refractory particles to high-enough temperatures for them to emit considerable grey body and blackbody radiation. LII can be used to quantify rBC carbon mass concentration in aerosols by detecting the emitted thermal radiation, which is approximately proportional to rBC mass. There are different instrumental approaches for LII using both pulsed lasers (Michelsen et al., 2015) and continuous-wave lasers, as in the commercially available Single Particle Soot Photometer (SP2, Droplet Measurement Technologies, Longmont, CO, USA). The SP2 quantifies the rBC mass in individual particles (Stephens et al., 2003; Schwarz et al., 2006; Moteki and Kondo, 2007). When aerosol particles enter the instrument, they are directed into the center of an intra-cavity Nd:YAG laser beam with a wavelength of 1064 nm where they are irradiated. BC-containing particles absorb the laser light causing them to heat up and incandesce. Since the thermal radiation emitted by individual black carbon particles is proportional to the volume (and mass) of BC in the particles (Moteki and Kondo, 2010), this radiation intensity can be converted to rBC mass using an empirical calibration curve.

2.3.2 rBC mass calibration

The relationship between incandescence signal peak amplitude and BC mass depends on the BC type (Moteki and Kondo, 2010; Laborde et al., 2012a), which means the instrument should be calibrated with a material that represents the type of BC one seeks to measure. Unfortunately, many types of BC are found in the atmosphere, such that it is typically not possible to calibrate the SP2 specifically with atmospheric BC. Instead, a fixed calibration using commercial BC materials is commonly applied. Therefore, potential variation in the chemical microstructure of atmospheric BC results in uncertainty in rBC mass measurements.

In this study, two different batches of fullerene soot (Alfa Aesar, stock 40971, lots FS12S011 and W08A039) were used. The former is recommended as calibration material (Baumgardner et al., 2012) since it was shown to be suitable for quantifying BC in diesel engine exhaust (agreement within 10 % for rBC cores ≤ 40 fg; Laborde et al., 2012b). Calibrations using the latter batch agreed with those using the former batch within 5 %. In this work, three different SP2 instruments (Paul Scherrer Institute, PSI; Institute des Géosciences de l'Environnement, IGE; Alfred Wegener Institute, AWI) were used to acquire the data (Table 3). This however does not contribute appreciably to uncertainties, since the reproducibility of measured rBC mass size distributions was shown to be ± 10 % during a large SP2 intercomparison involving six SP2 instruments from six different research groups (Laborde et al., 2012b). The SP2 used during the Melpitz campaigns was calibrated using an aerosol particle mass analyzer (APM) to select the calibration particles by mass (Table 3). For the other campaigns a differential mobility analyzer (DMA) was used for size selection and the corresponding particle mass was calculated using effective density data reported in Gysel et al. (2011). The latter approach results in an additional error of about 10 %.

2.3.3 Potential interferences and artifacts

One of the strengths of the SP2 is that the incandescence signal is not perturbed by the presence of non-refractory matter internally or externally mixed with BC (Moteki and Kondo, 2007; Slowik et al., 2007). However, other types of highly refractory and sufficiently light-absorbing (at 1064 nm) material can incandesce in the SP2 laser. Therefore, SP2 measurements can potentially contain interferences from metals, metal oxides (Moteki et al., 2017), volcanic ash and dust (rarely) (Kupiszewski et al., 2016). Fortunately, such materials are usually observed only rarely in atmospheric aerosols in large-enough quantities to cause significant SP2 measurement artifacts. Furthermore, if they are present, in some cases their presence can be identified and ignored when calculating rBC mass. Specifically, potential interference can be determined with the use of the spectral bandpass filters, which permits the determination of the color temperature of incandescence (Moteki et al., 2017). Recently, Sedlacek et al. (2018) found that rBC-free organic particles that absorb light at 1064 nm can char and form rBC under sufficiently high SP2 laser power, resulting in an rBC overestimate. In general, this artifact is only likely to be relevant in biomass burning plumes that contain organic tar balls that can absorb light at 1064 nm (Sedlacek et al., 2018). Marine engines operated with heavy fuel oil can also produce tar particles, but Corbin and Gysel-Beer (2019) found that the contribution of such particles to rBC mass was negligible. Furthermore, it is possible to distinguish incandescing tar particles from soot BC with SP2 measurements by examining the ra-

Table 2. Description of the methodology for EC mass concentration measurements: thermal protocol, sampling duration, inlet size cut, flow rate and performance during the ERLAP intercomparison, in relative terms for EC bias and variability (Sect. 2.2.3 and Eqs. S1 and S2).

Station code	Thermal protocol for m_{EC}	Sampling duration (h)	Inlet size cut	Flow rate	EC bias	EC variability
Palaiseau	EUSAAR-2 (TOT)	12	$PM_{2.5}$	$30\,m^3$ in 12 h	−6.0 %	11.9 %
Melpitz winter	EUSAAR-2 (TOT)	24	$PM_{2.5}$	$30\,m^3\,h^{-1}$	−6.0 %	4.3 %
Melpitz summer	EUSAAR-2 (TOT)	24	$PM_{2.5}$	$30\,m^3\,h^{-1}$	16.1 %	4.4 %
Cabauw	EUSAAR-2 (TOT)	12	PM_{10}	$27.6\,m^3$ in 12 h	−6.7 %	3.0 %
Bologna	EUSAAR-2 (TOT)	24	$PM_{2.5}$	$38.3\,L\,min^{-1}$	1.6 %	6.8 %

Table 3. Description of the measurement methodology for rBC mass concentration adopted during each campaign, along with SP2 owner (Paul Scherrer Institute (PSI), Alfred Wegner Institute (AWI) and Institut de Géosciences de l'Environment (IGE)), calibration material (fullerene soot batch), calibration method selection and inlet size cut.

Station code, campaign	SP2 owner	Revision, acquisition card type	Calibration material (fullerene soot batch)	Size selection method for calibration	Inlet size cut	SP2 upper detection limit [nm]
Palaiseau	PSI	*C*, 14 bit – 2.5 MHz – eight channels	Fullerene soot (stock 40971, lot FS12S011)	DMA	PM_{10}	439
Melpitz winter	AWI	*C*, 14 bit – 2.5 MHz – eight channels	Fullerene soot (stock 40971, lot W08A039)	APM	PM_{10}	722
Melpitz summer	PSI	*C*, 14 bit – 2.5 MHz – eight channels	Fullerene soot (stock 40971, lot FS12S011)	APM	PM_{10}	766
Cabauw	IGE	*C*, 14 bit – 2.5 MHz – eight channels	Fullerene soot (stock 40971, lot FS12S011)	DMA	PM_{10}	537
Bologna	PSI	*C*, 14 bit – 2.5 MHz – eight channels	Fullerene soot (stock 40971, lot FS12S011)	DMA	No size cut	676

tio of scattering-at-incandescence to incandescence signals (Corbin and Gysel-Beer, 2019).

2.3.4 SP2 detection efficiency and detection range

The SP2 lower detection limit depends on both physical limitations of the detection technique and instrument parameters chosen by the operator (Schwarz et al., 2010). With an optimal setup, the SP2 can reach unit counting efficiency for rBC mass of $m_{rBC} \approx 0.12$ fg (Schwarz et al., 2010; Laborde et al., 2012a), which corresponds to an rBC mass equivalent diameter of $D_{rBC} \approx 50$ nm using a void-free BC bulk density of $1800\,kg\,m^{-3}$ (Moteki and Kondo, 2010). The lower cut-off size for unit counting efficiency can be larger if the SP2 is not optimally set up. Usually the SP2's counting efficiency is robust down to $D_{rBC} \approx 80$ nm ($m_{rBC} \approx 0.48$ fg). We only considered the data of particles with BC cores greater than $D_{rBC} = 80$ nm in this study, as exact characterization of the cut-off curve was not performed in all campaigns. Note that poor counting efficiency for BC cores with greater mass than this limit has been reported by Gysel et al. (2012). Palas

soot, which is characterized by a very small primary sphere size and very low fractal dimension, results in relatively enhanced heat loss. However, we are not aware of studies indicating reduced counting efficiency for atmospherically relevant BC particles, which have larger primary spheres and a higher fractal dimension, compared to Palas soot.

The SP2 was operated downstream of inlets with a 50 % cut-off diameter at 10 µm in every campaign except for the Bologna campaign, where no external upper size cut was applied. In addition, the SP2 is unable to quantify rBC mass above a certain limit due to the saturation of the electronics that record the signals. This saturation limit can be varied via detector gains, with typical settings resulting in upper limits of quantification ranging from $D_{\mathrm{rBC}} \approx 500$ nm to around $D_{\mathrm{rBC}} \approx 1$ µm. Consequently, the total BC mass may be underestimated if BC cores greater than the upper limit of quantification contribute substantially to total BC mass. Recently, Schwarz (2019) evaluated an algorithm for reconstructing the peak incandescence intensity from the truncated incandescence signals of large BC cores. We did not apply this approach as it only allows increasing the upper limit of quantification by around 15 % in terms of D_{rBC} without introducing substantial uncertainty in the upper limit of quantification.

The SP2 has no lower number concentration detection limit (in the absence of leaks), while particle counting coincidence imposes an upper concentration limit when multiple BC particles cross the laser beam simultaneously. Coincidence only caused negligibly low bias in measured rBC mass concentrations for the concentration ranges that were encountered in this study.

2.3.5 Methods to correct SP2 data for missing mass below lower detection limit (LDL)

Two approaches are most commonly used to extrapolate the measured rBC mass size distribution and correct for the missing rBC mass (Schwarz et al., 2006; Laborde et al., 2013). In this study, both methods were applied in order to assess the sensitivity to the correction approach (Sect. 3.1); based on this assessment the first of the two methods described below was determined to be preferable. The two methods are based on fitting the measured rBC mass size distribution with a unimodal lognormal function since BC mass size distributions are generally close to lognormally distributed (e.g., Fig. 1; Schwarz et al., 2006; and Reddington et al., 2013).

A first approach to correcting SP2 rBC measurements for potentially missed mass is based on extrapolation of the measured size distribution below and/or above the SP2 detection limits. We hereafter refer to this as the "extrapolation method". The corrected rBC mass, $m_{\mathrm{rBC,corr}}^{\mathrm{extrap}}$, is obtained as the sum of the measured mass, $m_{\mathrm{rBC,meas}}$, and a correction term, $\Delta m^{\mathrm{extrap}}$:

$$m_{\mathrm{rBC,corr}}^{\mathrm{extrap}} = m_{\mathrm{rBC,meas}} + \Delta m^{\mathrm{extrap}}. \quad (1)$$

Here, $\Delta m^{\mathrm{extrap}}$ is obtained by fitting a lognormal function $\frac{\mathrm{d}m_{\mathrm{fit}}}{\mathrm{dlog}D_{\mathrm{rBC}}}$ to the measured rBC mass size distribution and only considering potentially missed mass below the lower detection limit (LDL) of the SP2. No correction was applied for potentially missed mass above the upper detection limit (UDL) for two reasons explained in Sect. 3.1.1. Using this approach, the correction term simplifies to the integrated mass of the lognormal fit in the size range below the LDL:

$$\begin{aligned}\Delta m^{\mathrm{extrap}} &= \Delta m_{\mathrm{rBC<LDL}} \\ &= \int_0^{D_{\mathrm{LDL}}} \frac{\mathrm{d}m_{\mathrm{fit}}}{\mathrm{dlog}D_{\mathrm{rBC}}}(D_{\mathrm{rBC}})\,\mathrm{dlog}D_{\mathrm{rBC}}. \end{aligned} \quad (2)$$

A second commonly applied approach, hereafter referred to as the "fit method", is based on the assumption that the true BC mass size distribution in the submicron size range exactly follows a lognormal function. Under this assumption, the corrected rBC mass, $m_{\mathrm{rBC,corr}}^{\mathrm{fit}}$, is chosen as the integrated mass, m_{fit}, of a lognormal fit to the measured rBC mass size distribution (which includes corrections for contributions below the LDL and above the UDL):

$$m_{\mathrm{rBC,corr}}^{\mathrm{fit}} = m_{\mathrm{fit}} = \int_0^{+\infty} \frac{\mathrm{d}m_{\mathrm{fit}}}{\mathrm{dlog}D_{\mathrm{rBC}}}(D_{\mathrm{rBC}})\,\mathrm{dlog}D_{\mathrm{rBC}}. \quad (3)$$

The corrected BC mass obtained with this second approach is composed of four terms (Eq. 4), which are visualized in Fig. 1: (i) the measured rBC mass, $m_{\mathrm{rBC,meas}}$ (black solid line); (ii) the rBC mass below the SP2 detection limit, $\Delta m_{\mathrm{rBC<LDL}}$ (red shading; Eq. 2); (iii) the rBC mass above the SP2 detection limit, $\Delta m_{\mathrm{rBC>UDL}}$ (blue shading; Eq. 5); and (iv) the residual area between the fit, m_{fit} and the measured rBC mass integrated in the range from D_{LDL} to D_{UDL} (denoted as $\Delta m_{\mathrm{fitresid}}$; purple shading; Eq. 6):

$$\begin{aligned} m_{\mathrm{rBC,corr}}^{\mathrm{fit}} &= \Delta m_{\mathrm{rBC<LDL}} + \Delta m_{\mathrm{rBC>UDL}} \\ &\quad + m_{\mathrm{rBC,meas}} + \Delta m_{\mathrm{fitresid}}, \end{aligned} \quad (4)$$

where

$$\Delta m_{\mathrm{rBC>UDL}} = \int_{D_{\mathrm{UDL}}}^{+\infty} \frac{\mathrm{d}m_{\mathrm{fit}}}{\mathrm{dlog}D_{\mathrm{rBC}}}(D_{\mathrm{rBC}})\,\mathrm{dlog}D_{\mathrm{rBC}} \quad (5)$$

and

$$\begin{aligned}\Delta m_{\mathrm{fitresid}} &= \int_{D_{\mathrm{LDL}}}^{D_{\mathrm{UDL}}} \frac{\mathrm{d}m_{\mathrm{fit}}}{\mathrm{dlog}D_{\mathrm{rBC}}}(D_{\mathrm{rBC}}) \\ &\quad - \frac{\mathrm{d}m_{\mathrm{meas}}}{\mathrm{dlog}D_{\mathrm{rBC}}}(D_{\mathrm{rBC}})\,\mathrm{dlog}D_{\mathrm{rBC}}. \end{aligned} \quad (6)$$

Note that with this definition $\Delta m_{\mathrm{fitresid}}$ has a negative value for the example shown in Fig. 1. The correction term in the case of the fit method is naturally defined as the difference between the corrected and the measured rBC mass:

$$\Delta m^{\mathrm{fit}} = m_{\mathrm{fit}} - m_{\mathrm{rBC,meas}}. \quad (7)$$

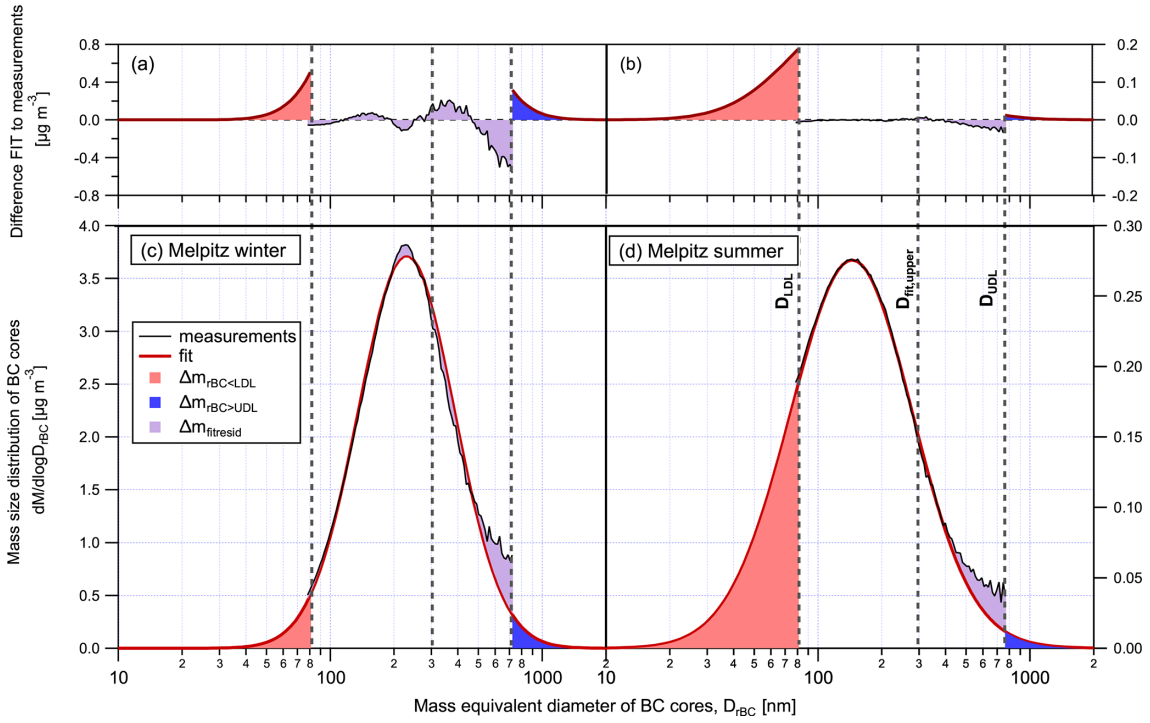

Figure 1. Approach to correct for the rBC mass outside the rBC core size range covered by the SP2 for the Melpitz winter (**a** and **c**) and the Melpitz summer (**b** and **d**) campaigns. **(c)** and **(d)** show the measured rBC mass size distribution as a function of rBC core mass equivalent diameter, including the SP2 detection limits D_{LDL} and D_{UDL}. The lognormal functions are fitted between D_{LDL} and $D_{\mathrm{fit,upper}}$. The integrated areas of the red, purple, and blue shading correspond to $\Delta m_{\mathrm{rBC<LDL}}$, $\Delta m_{\mathrm{fitresid}}$ and $\Delta m_{\mathrm{rBC>UDL}}$, respectively (see Sect. 2.3.5). **(a)** and **(b)** additionally show the same shading after subtraction of the measured size distribution (and measurement forced to be zero outside the SP2 detection range). The average mass size distributions of the other campaigns are represented in Fig. S1.

From Eqs. (4) and (7), one can derive:

$$\Delta m^{\mathrm{fit}} = \Delta m_{\mathrm{rBC<LDL}} + \Delta m_{\mathrm{rBC>UDL}} + \Delta m_{\mathrm{fitresid}}. \quad (8)$$

Comparing the missing mass correction terms of the two approaches given in Eqs. (1) and (4) shows that the corrected rBC mass differs by the sum of two physically meaningful quantities, the fit residual and the extrapolated rBC mass above the UDL:

$$m^{\mathrm{fit}}_{\mathrm{rBC,corr}} - m^{\mathrm{extrap}}_{\mathrm{rBC,corr}} = \Delta m_{\mathrm{rBC>UDL}} + \Delta m_{\mathrm{fitresid}}. \quad (9)$$

The results of these two approaches are compared and discussed in relation to the different datasets used in this study in Sect. 3.1.1. Outside of Sects. 3.1.1 and 3.1.2, Figs. 1, 2 and S1, and Table 4, this paper applies the first method (Eq. 1) to quantify rBC mass.

2.4 Auxiliary measurements

2.4.1 Aerosol size distribution

In the Melpitz winter and summer campaigns, aerosol number size distributions in the diameter range from 3.8 to 770 nm were measured with a mobility particle size spectrometer (MPSS), custom built by Wiedensohler et al. (2012), which consists of a differential mobility analyzer (DMA) and a condensation particle counter (CPC). The DMA was operated with a sheath airflow of 10 L min^{-1}, and the aerosol number size distribution was measured every 20 min. During the Cabauw campaign, a modified version of a commercially available scanning mobility particle sizer (TSI SMPS 3034) provided the number size distribution of the aerosol in the diameter range from 10 to 470 nm. No size information is available for the Palaiseau and Bologna campaigns.

2.4.2 Absorption Ångström exponent (AAE) inferred from Aethalometer data

The Aethalometer measures the light attenuation through a sample filter that is continuously loaded with aerosol (Hansen et al., 1984). The raw attenuation coefficient (b_{atn}) is calculated from the rate of attenuation change with time. The relationship between the attenuation coefficient and absorption coefficient of the deposited aerosol particles is linear for low attenuation values, but saturation occurs when the attenuation values are high (Weingartner et al., 2003). Therefore, the measurements must be corrected for this "loading effect" in order to obtain a corrected attenuation coefficient

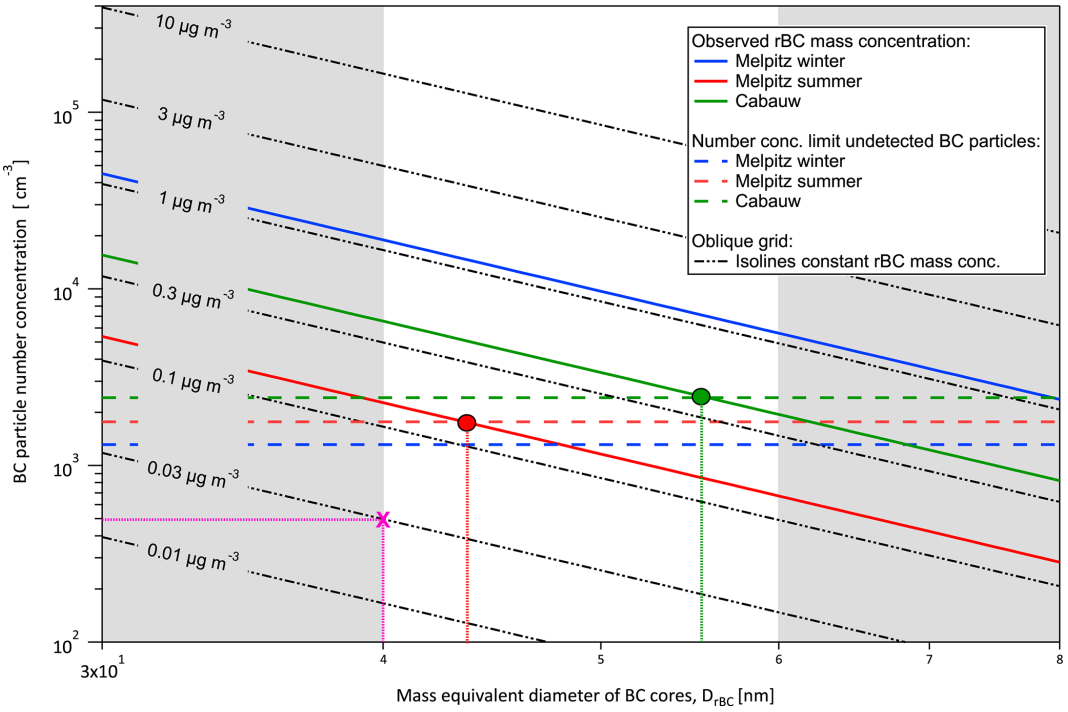

Figure 2. Relationship between rBC mass equivalent diameter, BC particle number concentration and rBC mass concentration for perfectly monodisperse BC aerosols (magenta cross and lines illustrate an example of this unambiguous relationship). The oblique dash-dotted black grid represents isolines of constant rBC mass concentration. The continuous oblique lines represent the observed uncorrected rBC mass concentrations (campaign geometric mean values). The horizontal dashed lines represent the upper number concentration limit (n_{limit}), calculated as the difference between the assumed maximum and the measured BC particle number concentration. The figure can be read in two ways: the intersects of the horizontal lines with rBC mass concentration isolines provide an upper limit for the maximal undetected rBC mass concentration if the undetected mode peaks at the diameter where the intersect occurs. Alternatively, when the horizontal dashed line crosses the corresponding oblique line of the same color (e.g., red point if we consider Melpitz summer), this corresponds to a maximal contribution of rBC mass concentration in small undetected particles equal to the observed value. If we consider Melpitz summer as an example (red point) this happens for a BC mass mode of 44 nm. The grey shading indicates that the modal diameter of a hypothetical mode undetected by the SP2 is expected to be between 40 and 60 nm.

Table 4. Estimates of potentially missed rBC mass for the two methods ($\Delta m^{\mathrm{extrap}}$ and Δm^{fit}), summands contributing to it ($\Delta m_{\mathrm{rBC>UDL}}$ and $\Delta m_{\mathrm{fitresid}}$) and modal diameter of the averaged rBC mass size distribution, all separately listed for each campaign. The size range of 80–300 nm rBC mass equivalent diameter was chosen for fitting the measurement. The sensitivity of the results to this choice was negligible, as discussed in the text.

	Mass fractions				
Campaigns	$\Delta m^{\mathrm{extrap}}$ [%] ($:= \Delta m_{\mathrm{rBC<LDL}}$)	Δm^{fit} [%]	$\Delta m_{\mathrm{rBC>UDL}}$ [%]	$\Delta m_{\mathrm{fitresid}}$ [%]	$D_{\mathrm{rBC,mode}}$ [nm]
Bologna	24.1 ± 6.4	17.8 ± 7.4	0.2 ± 0.3	-6.5 ± 1.9	118.6 ± 0.3
Cabauw	22.4 ± 4.9	19.7 ± 4.6	0.7 ± 0.3	-3.4 ± 1.0	127.2 ± 0.4
Melpitz summer	24.5 ± 8.5	20.5 ± 7.3	0.4 ± 0.3	-4.5 ± 3.7	142.9 ± 0.3
Melpitz winter	2.9 ± 2.1	2.5 ± 1.4	1.1 ± 0.4	-1.5 ± 1.5	227.9 ± 0.7
Palaiseau	20.3 ± 8.7	18.0 ± 7.0	2.5 ± 2.0	-4.9 ± 2.1	136.7 ± 0.3

($b_{\mathrm{atn,corr}}$) (Virkkula et al., 2007; Drinovec et al., 2015). The attenuation coefficient is greater than the absorption coefficient due to multi-scattering effects within the filter matrix, described with a proportionality constant C.

From a pair of $b_{\mathrm{atn,corr}}$ coefficients at two different wavelengths, λ_1 and λ_2, it is possible to calculate the absorption Ångström exponent, AAE(λ_1, λ_2), a coefficient commonly used to describe the spectral dependence of the aerosol light absorption coefficient (Moosmüller et al., 2009):

$$\mathrm{AAE}(\lambda_1, \lambda_2) = -\frac{\ln(b_{\mathrm{atn,1,corr}}(\lambda_1))}{\ln(b_{\mathrm{atn,1,corr}}(\lambda_2))}\frac{\ln(\lambda_2)}{\ln(\lambda_1)}. \quad (10)$$

Note that since the Aethalometer C value has only a small spectral dependence (Weingartner et al., 2003; Corbin et al., 2018), it is possible to infer the AAE directly from the corrected attenuation coefficient, as is done in this work.

The AAE provides an indication of the sources of BC (Zotter et al., 2017). The light absorption of particles from traffic emissions is dominated by BC, which has an AAE of ~ 1. By contrast, wood burning emissions contain a mixture of BC and co-emitted brown carbon. Light absorption by brown carbon has a much stronger spectral dependence than BC, such that the mixture has an AAE of between ~ 1 and 3 (Kirchstetter et al., 2004; Corbin et al., 2018). This makes relative apportionment of BC to traffic and wood burning sources based on the aerosol AAE possible. However, this simple approach only works in the absence of additional BC sources or light-absorbing aerosol components (e.g., from coal combustion).

In this paper the AAE values were calculated with the formula presented in Eq. (10) with $\lambda_1 = 470$ nm and $\lambda_2 = 950$ nm. Aethalometer AE31 (Magee Scientific) instruments were used during the Palaiseau and Cabauw campaigns. These measurements were corrected for the loading effect with the algorithm developed by Weingartner et al. (2003). In the other campaigns, Aethalometer AE33 (Magee Scientific) instruments were used. These data did not need further correction since the algorithm developed by Drinovec et al. (2015), which takes into account the filter loading effect, is incorporated into the instrument. However, the AE33 firmware correction was not working properly during the Bologna campaign. Therefore, these data were corrected using the Weingartner et al. (2003) correction.

3 Results and discussion

3.1 Mass of rBC potentially missing below the LDL of the SP2

3.1.1 Comparison of two approaches to correct for the truncated rBC mass

In the following, we compare the results from the two different approaches for estimating the missing rBC mass concentration outside the size range covered by the SP2 (see Sect. 2.3.5).

Typically, the measured size distributions only approximately followed a lognormal distribution. We chose to infer and present the missed rBC mass estimate based on fitting across the range from 80 to 300 nm. In addition, the sensitivity to the fitted range was assessed. The estimated missed rBC mass below the SP2 LDL increased by up to 11 % of the measured mass when increasing the lower fit limit from 80 to 100 nm, i.e., around the SP2 LDL. This provides evidence that the extrapolation towards the smallest BC cores is not strongly affected by the SP2 counting efficiency performance, which could potentially be degraded in this range. The fit approach used the total area of a lognormal fit to rBC mass size distributions to obtain the correct rBC mass. Sensitivity analyses performed with fitting to a manually prescribed upper limit between 200 and 400 nm showed that the fit results were insensitive to the choice of this upper limit for valid fits. Therefore, a fixed fit range from 80 to 300 nm, which always provides a good match between the measured and fitted size distribution around the mode of the distribution, will be used in the remainder of this paper for missing mass corrections. The validity of the fits was determined by comparing the fitted peak location with the mode of the measured data. Data were only fitted to a manually prescribed upper limit, and the fit results were insensitive to the choice of this upper limit for valid fits, while larger deviations occurred for invalid fits.

Detailed results of the missing mass correction are listed in Table 4. The extrapolation method and the fit method provide comparable results. It can be seen that $\Delta m^{\mathrm{extrap}}$ varied in the range of 3 %–25 %, while Δm^{fit} varied between 3 %–21 %. Considerable variability in missing mass correction between campaigns occurred due to differences in the rBC mass size distribution, especially differences in the average modal diameters, which are also listed in Table 4. As shown in Eq. (9), the extrapolation and the fit methods for missing mass correction differ by the sum of the fit residual ($\Delta m_{\mathrm{fitresid}}$) and the extrapolated mass above the UDL ($\Delta m_{\mathrm{rBC>UDL}}$). The opposite signs and comparable magnitudes of these two terms (Table 4), shown as purple and blue shading in Figs. 1 and S1, have partially compensating effects, resulting on average in only a 3 % difference between the two missing mass correction methods.

The systematic difference between measurement and fit for rBC mass equivalent diameters near the UDL of the SP2 (Figs. 1 and S1) could indicate either the presence of a second lognormal mode that is centered at a larger diameter than the main mode or an inaccurate extrapolation of the incandescence signal calibration for masses greater than 64 fg ($D_{\mathrm{rBC}} = 408$ nm). As both effects make extrapolation of the rBC mass size distribution above the UDL uncertain, we decided to apply the extrapolation method in this study. As explained in Sect. 2.3.5 (Eqs. 1 and 2), the extrapolation method only uses the fit below the LDL of the SP2 to esti-

mate missing rBC mass. This ensures a well-defined upper cut-off in terms of rBC core mass for the corrected rBC mass concentration results. In the following, all reported rBC mass concentrations are corrected with the extrapolation method (Eq. 2) with the fit range chosen from 80 to 300 nm, unless otherwise stated.

The missing mass correction results for the Melpitz winter campaign are significantly different from those for the Melpitz summer campaign and all other campaigns (Figs. 1, S1 and Table 4). Specifically, the missed mass percentage for the Melpitz winter campaign is less than 3 %, while it is between 18 % and 24.5 % for the other campaigns. This is due to the fact that the Melpitz winter rBC core mass size distribution peaks in the middle of the SP2 detection range, with $D_{\mathrm{rBC,mode}} = 227.9$ nm (Fig. 1 and Table 4). This is not the case for the other campaigns, where, as shown in Table 4, the average rBC mass size distributions have their maximum between 118.6 and 142.9 nm (Figs. 1 and S1). This could indicate that in Melpitz during the winter the BC source was different from that of the other campaigns of this work. Indeed, with a back-trajectory analysis on the same dataset, Yuan et al. (2021) showed that the period between 5 and 14 February 2017 was characterized by air masses transported from southeast Europe, where coal is still used as fuel (Spindler et al., 2013). Coal combustion and biomass burning produce rBC size distributions with larger modal diameter than traffic emissions (Bond et al., 2013; Liu et al., 2014; Schwarz, 2019).

3.1.2 Limits to rBC mass missed in small BC cores imposed by the BC particle number

The presence of an additional mode of small particles below the lower detection limit of the SP2 would introduce an error in the above extrapolation calculations. Indeed, a substantial fraction of nascent soot particles emitted by combustion engines is usually below the detectable size range of the SP2. Count median diameters (CMDs) of nonvolatile particle size distributions in aircraft turbine exhaust range from 15 to 40 nm (Lobo et al., 2015; Durdina et al., 2017, 2019) while unfiltered gasoline direct injection and diesel engines have larger CMD values ranging from 50 to 100 nm (Burtscher et al., 2001; Momenimovahed and Olfert, 2015).

The existence of additional modes of BC cores at diameters below the SP2 lower detection limit has been hypothesized based on the observation of "upticks" in rBC mass size distributions at the LDL of the SP2 (i.e., increasing particle concentration with decreasing mass equivalent diameter as the SP2 LDL is approached) (Liggio et al., 2012; Cappa et al., 2019). Cappa et al. (2019) performed multi-modal fits to measured SP2 size distributions with upticks assuming a fixed modal diameter (47 nm) and geometric standard deviation (1.63) of the lognormal mode lying below the SP2 LDL. These authors estimated that the campaign average mass concentration of the hypothesized small mode of BC particles was as large as 52 % of the total measured rBC mass concentration. While upticks at the lower end of SP2 size distributions may indicate the presence of an additional mode of small rBC particles, it should be noted that these upticks might also represent measurement artifacts. SP2 measurements of rBC cores with diameters below 100 nm are sensitive to small variations in fitted calibration curves, and it is difficult to perform accurate calibration measurements near the LDL of the SP2 (Laborde et al., 2012a). Nevertheless, we cannot exclude the presence of an undetected mode with a small modal diameter between around a 40 and 60 nm BC core size in our studies. An even smaller mode diameter is considered unlikely because such small particles can be found only in the proximity of a source (Zhu et al., 2006). A larger mode diameter is unrealistic in our campaigns because we did not see any sign of the upper tail of such a hypothetical mode at the bottom end of the BC size distribution measured by the SP2.

The mass of BC particles below the lower detection limit of the SP2 ($D_{\mathrm{rBC}} < \sim 80$ nm) can be estimated by measuring the total number concentration of nonvolatile particles by thermo-denuded MPSS measurements, assuming that BC particles dominate the number of nonvolatile (NV) particles remaining after thermal treatment (Clarke et al., 2004). Miyakawa et al. (2016) employed this approach to conclude that the fraction of small rBC particles with D_{rBC} less than around 80 nm did not contribute substantially to the total rBC mass concentrations measured at an industrial site south of Tokyo, Japan. In the absence of such thermally treated measurements, we assume 30 % of total measured particle number concentration as an upper limit for total BC particle number concentration (Wehner et al., 2004; Reddington et al., 2013; Cheung et al., 2016). This provides, after subtraction of the BC particle number concentration measured by the SP2, an upper limit (n_{limit}) for the undetected BC particle number concentration.

The three quantities of BC particle number concentration, rBC mass concentration and rBC mass equivalent diameter are unambiguously related for a hypothetical perfectly monodisperse mode of BC particles. This relationship is illustrated in Fig. 2, which presents BC number concentration versus rBC mass equivalent diameter along with isolines of constant rBC mass concentration (dash-dotted lines). For example, the magenta marker indicates that a BC particle number concentration of 494 cm^{-3} and rBC core diameter of 40 nm translates to an rBC mass concentration of 0.03 $\mu\mathrm{g\,m}^{-3}$. The horizontal dashed lines in Fig. 2 indicate the estimated upper limit, n_{limit}, for the BC particle number undetected by the SP2. Taking the Melpitz winter campaign as an example, the dashed blue line is clearly below the oblique continuous blue line in the BC core range between 40 and 60 nm. Comparing the rBC mass concentrations corresponding to these two lines at a 40 and 60 nm diameter shows that the maximal undetected rBC mass concentration associated with small BC cores is at most 7 % to 23 %

of the measured rBC mass concentration for modes peaking within these size limits. For Cabauw, the number limit and mass concentration lines cross at 55.5 nm (green point). The intersect implies that an undetected mode peaking at this size could at most contribute as much additional rBC mass as measured by the SP2. The constraints resulting for undetected modes between 40 and 60 nm are an additional 37 % and 125 % of observed rBC mass, respectively. For the Melpitz summer campaign, the number limit only provides a very weak constraint on the missed mass as the intercept occurs at 43.5 nm (red point). Therefore, the undetected rBC mass could reach up to 263 % of detected rBC mass if the modal diameter was located at 60 nm.

Based on the discussion in Sect. 3.1.1, in this study we applied the extrapolation method to correct for estimated rBC mass below the SP2 LDL (Δm^{extrap} in Table 4). The resulting corrections are smaller than the upper limit imposed by the BC particle number as discussed here. Hence, it cannot be excluded that the truly missed mass was larger than accounted for. The conservative estimate based on the BC particle number considerations suggests that the missing mass could be as large as 23 % (applied correction 3 %), 125 % (applied correction 22 %) and 263 % (applied correction 25 %) for the Melpitz winter, Cabauw and Melpitz summer campaigns, respectively.

3.2 Comparison of observed EC and rBC mass concentrations

Here we aim at achieving a quantitative comparison of rBC (after correction using Eq. 1) and EC mass concentrations measured by the SP2 and the thermal–optical method, respectively. Figure 3 shows a scatterplot of time-resolved data using distinct colors for each campaign (rBC data averaged according to the sampling periods of the EC samples). Figure S2 presents the corresponding statistics of the rBC-to-EC mass ratio, and Table 5 reports all statistical parameters. The median values of the rBC-to-EC mass ratio lie between the arithmetic and geometric means, indicating distributions that are between the normal and lognormal distribution (Fig. S2). For this reason, we adopted the median when reporting the ratio of the two quantities and in the figures (lines in Figs. 3 and 6) and the geometric standard deviation (GSD) to report the $m_{\text{rBC}}/m_{\text{EC}}$ variability (Table 5). Considering all data points from all campaigns, the median value of $m_{\text{rBC}}/m_{\text{EC}}$ was 0.92 with a GSD of 1.5. That is, m_{rBC} was on average 8 % smaller than m_{EC}, and 68 % of the individual data points fell into the range within a factor of 1.5 around the geometric mean ratio. Accordingly, the overall statistics for these two quantities agree closely, with geometric mean values (GSD) of 0.41 (2.60) and 0.47 (2.46) $\mu g\,m^{-3}$ for m_{rBC} and m_{EC}, respectively, both ranging from 0.05 to 3.22 $\mu g\,m^{-3}$ (Fig. 3).

The above result suggests a very small overall systematic bias between rBC and EC mass on average. However, a look at the statistics calculated for each campaign separately (Table 5 and Fig. S2) reveals a slightly different picture: the variability in the rBC-to-EC mass ratio is considerably smaller for individual campaigns, with GSDs typically around 1.2–1.3, and the systematic bias on the campaign level is substantially greater than the overall bias, with median ratios ranging from 0.53 to 1.29. During the Melpitz winter campaign, m_{rBC} was on average 29 % higher than m_{EC} with m_{rBC} and m_{EC} geometric means (GSD) of 1.20 (2.64) and 0.97 (2.16) $\mu g\,m^{-3}$, respectively. During the Melpitz summer campaign, m_{rBC} was comparable to m_{EC} within 3 %, with respective geometric means (GSD) of 0.17 (1.57) and 0.18 (1.54) $\mu g\,m^{-3}$. For the Bologna summer campaign, the median rBC-to-EC mass ratio was 0.65, with m_{rBC} and m_{EC} geometric means (GSD) of 0.40 (1.46) and 0.64 (1.45) $\mu g\,m^{-3}$. The largest difference was found in Cabauw, with a median rBC-to-EC mass ratio of 0.53 and geometric means (GSD) of m_{rBC} and m_{EC} of 0.46 (1.62) and 0.86 (1.63) $\mu g\,m^{-3}$, respectively. During the Palaiseau campaign, m_{rBC} was 20 % higher than m_{EC}; this value is somewhat higher than the value of 15 % previously published in Laborde et al. (2013), which is explained by the fact that here we used the $m_{\text{rBC}}/m_{\text{EC}}$ median value instead of the result of the linear fit.

3.3 Discussion of level of agreement between the rBC and EC mass concentration measurements

In this section, we test different hypotheses for the observed differences between rBC and EC mass.

3.3.1 Differences in upper cut-off diameters and in inlet losses

Differences in the upper cut-off diameters for the EC and rBC mass measurements are a potential source of discrepancy. The EC mass measurements presented in Fig. 3 relate to an upper 50 % cut-off at an aerodynamic particle diameter $D_{\text{aero}} = 2.5\,\mu m$ at ambient RH (Table 2), except for Cabauw, where a PM_{10} inlet was used. The SP2 measurements were mostly taken behind PM_{10} inlets. However, the SP2 has a more stringent intrinsic UDL, which varied from $D_{\text{UDL}} = 439$ to $D_{\text{UDL}} = 766$ nm BC core mass equivalent diameter, depending on the campaign (Table 3). To explore the possibility that BC particles with diameters between the UDL of the SP2 and 2.5 µm aerodynamic diameter contributed to the discrepancies between m_{rBC} and m_{EC}, the SP2-related mass equivalent diameters (D_{ve}) were converted to aerodynamic diameters (D_{aero}). This was carried out by numerically solving Eq. (11), where C_{C} is the Cunningham slip correction factor, ρ_{p} is the particle density, $\rho_0 = 1000\,kg\,m^{-3}$ and χ is the particle dynamic shape factor (more details in Sects. S3 and S4 of the Supplement):

$$D_{\text{ve}} = D_{\text{aero}} \sqrt{\frac{\rho_o \chi C_{\text{C}}(D_{\text{aero}})}{\rho_{\text{p}} C_{\text{C}}(D_{\text{ve}})}}. \quad (11)$$

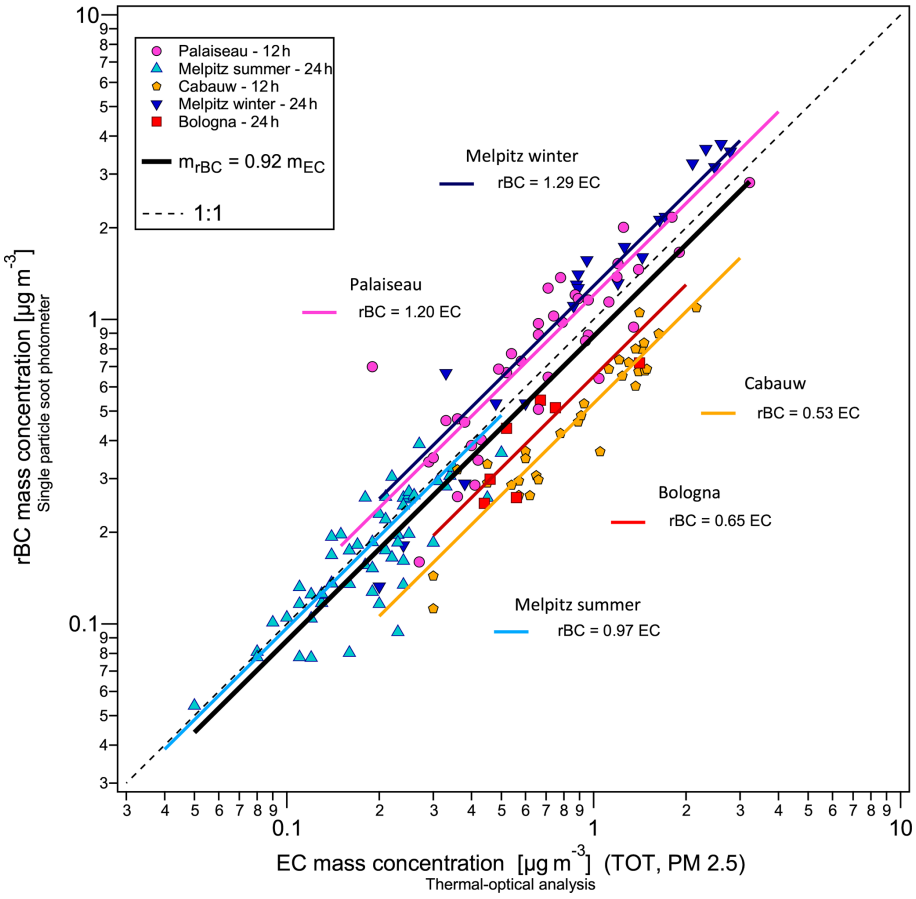

Figure 3. The rBC mass concentration versus EC mass concentration for the five campaigns studied in this paper. The median rBC-to-EC mass ratios are shown as lines for each campaign. Uncertainties in EC measurements as a function of EC and TC filter surface loadings as well as EC-to-TC mass ratio are presented in Fig. S3 and discussed in Sect. 3.3.2.

During the Melpitz winter campaign, the intrinsic UDL was at $D_{rBC} = 722$ nm. The aerodynamic diameter of externally mixed bare BC cores of this size varies from around $D_{aero} =$ 625 nm for fractal-like shapes to 970 nm for compact shapes (Table S3). For coated BC particles, the corresponding dry aerodynamic diameter ranges from around 1140 to 1660 nm for coating-to-core mass ratios of 1 : 1 and 6 : 1, respectively. The actual BC mixing state was measured by Yuan et al. (2021), though at smaller core diameters. Using these data as a constraint provides around 1320 nm as a best estimate for the dry aerodynamic diameter. However, the impactor for the filter sampling is operated at ambient RH, which means that hygroscopic growth affects the cut-off diameter. Potential hygroscopic growth was assessed as described in Sect. S4. Accordingly, the aerodynamic diameter of particles with BC core sizes at the SP2 UDL increases to up to 1610 and 2230 nm at 80 % and 95 % RH, respectively, for the best-estimate BC mixing state. Externally mixed bare BC particles are not affected by hygroscopic growth. Based on this analysis, it can be expected that the intrinsic SP2 UDL translates to a cut-off varying between PM_1 and $PM_{2.5}$ or even slightly smaller or greater under extreme assumptions. This statement also applies for the Melpitz summer campaign, where the SP2 UDL differed only marginally from that of the Melpitz winter campaign (Table 3).

Since during the Melpitz campaigns the EC mass concentrations were measured behind both PM_1 and $PM_{2.5}$ inlets, we were able to calculate the fraction of EC mass in particles with aerodynamic diameters between 1 and 2.5 µm out of the total EC mass in $PM_{2.5}$. Figure 4a and b indicate that between 10 % and 60 % of EC $PM_{2.5}$ mass was present in the large size fraction (1–2.5 µm, indicated as $EC_{2.5-1}$) for the majority of measurements during both the Melpitz winter and summer campaigns. These $EC_{2.5-1}$ fractions are greater than the longer-term average values at the Melpitz site, which is potentially related to the fact that coal combustion was a likely source of EC particles with diameters between 1 and 2.5 µm at the Melpitz site, at least during the winter campaign (van Pinxteren et al., 2019; Yuan et al., 2021).

The fact that the $EC_{2.5-1}$ fraction contributed on average around 30 % to 40 % EC mass in $PM_{2.5}$ during the Melpitz campaigns and that the SP2 BC particle cut-off is likely be-

Table 5. The m_{rBC} and m_{EC} statistics per campaign: median, arithmetic and geometric mean, geometric standard deviation (GSD), standard deviation (SD), 10th and 90th percentiles, and number of data points.

	Palaiseau	Cabauw[a]	Melpitz summer	Melpitz winter	Bologna	All the campaigns
m_{rBC} median (10th, 90th) [μg m^{-3}]	0.85 (0.34, 1.55)	0.47 (0.27, 0.83)	0.17 (0.09, 0.29)	1.41 (0.29, 3.56)	0.44 (0.26, 0.61)	0.41 (0.13, 1.44)
m_{EC}[a] median (10th, 90th), [μg m^{-3}]	0.71 (0.32, 1.36)	0.92 (0.45, 1.47)	0.19 (0.11, 0.31)	0.92 (0.45, 1.47)	0.56 (0.45, 1.01)	0.47 (0.14, 1.44)
m_{rBC} geometric mean (GSD), [μg m^{-3}]	0.77 (1.88)	0.46 (1.62)	0.17 (1.57)	1.20 (2.58)	0.40 (1.46)	0.41 (2.60)
m_{EC} geometric mean (GSD), [μg m^{-3}]	0.68 (1.83)	0.86 (1.63)	0.18 (1.54)	0.97 (2.16)	0.64 (1.45)	0.47 (2.46)
m_{rBC}/m_{EC} geometric mean (GSD)	1.13 (1.40)[b]	0.53 (1.19)	0.92 (1.26)	1.23 (1.32)	0.63 (1.23)	0.88 (1.50)
m_{rBC}/m_{EC} arithmetic mean (SD)	1.20 (0.51)	0.54 (0.11)	0.95 (0.24)	1.28 (0.33)	0.65 (0.14)	0.96 (0.41)
m_{rBC}/m_{EC} median (10th, 90th)	1.20 (0.72, 1.50)	0.53 (0.44, 0.64)	0.97 (0.63, 1.23)	1.29 (0.76, 1.58)	0.65 (0.49, 0.82)	0.92 (0.51, 1.42)
No. data points	39	32	55	21	7	154

[a] EC mass was measured in $PM_{2.5}$, except for the Cabauw campaign, where PM_{10} samples were collected.
[b] The statistics of the rBC-to-EC mass ratio for the Palaiseau campaign is strongly influenced by one outlier (see Fig. 3). Ignoring this outlier would provide a geometric mean ratio of 1.09 and a GSD of 1.32.

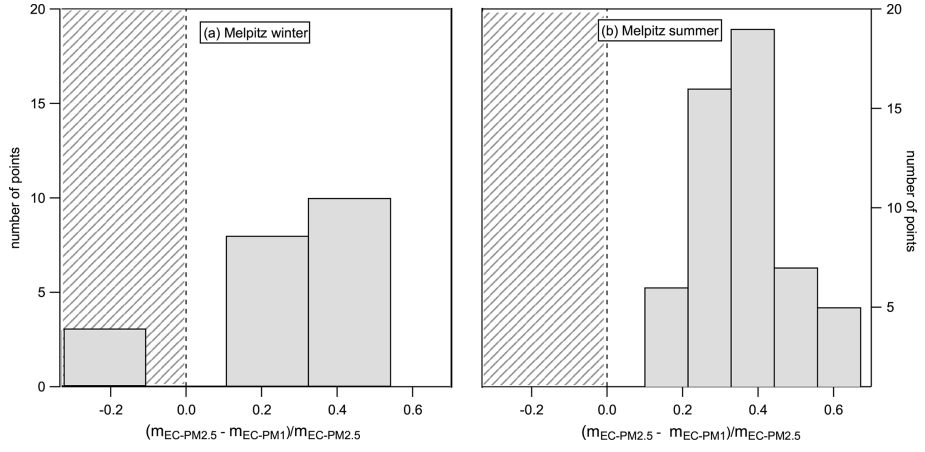

Figure 4. Histogram of $(m_{EC–PM2.5} - m_{EC–PM1})/m_{EC–PM2.5}$ for Melpitz winter (**a**, on the left) and summer (**b**, on the right) campaigns. The area with the oblique grey lines indicates the non-physical part in which $m_{EC–PM2.5} < m_{EC–PM1}$, reflecting the uncertainty in the EC measurements.

tween PM_1 and $PM_{2.5}$ makes it possible that differences related to the upper cut-off contribute to the discrepancies between measured rBC and EC mass seen in Fig. 3. However, additional covariance analyses of the $EC_{2.5-1}$ fraction with the rBC-to-EC bias did not provide a conclusive result. Furthermore, such cut-off effects should rather result in an rBC mass being lower than the EC mass, opposite to the result for the Melpitz winter campaign. This indicates the presence of other effects and biases, which over-compensated for the mass between 1 and 2.5 µm that the SP2 was not able to detect.

Concerning Cabauw, the $EC_{2.5-1}$ fraction could be a potential cause of the observed low rBC-mass-to-EC-mass ratio, given that EC was measured behind a PM_{10} inlet and that the SP2 cut-off was at $D_{rBC} = 537$ nm, resulting in a wider upper cut-off gap than during the other campaigns. However, the rBC modal diameter measured by the SP2 was the second lowest of all campaigns (Table 4 and Fig. S1), which makes a potential bias originating from the lower end of the BC size distribution more likely. A closer assessment is however not possible as no PM_1 EC samples are available, which also applies for the other sites.

Differences between m_{rBC} and m_{EC} can also come from differences in the inlet line losses. Particle losses can be caused by the presence of a dryer in the inlet line to which the SP2 was connected. In this work, the dryer losses are estimated to be less than 10 % (see further details in Sect. S5). Although this is, therefore, not the major contributor to the observed discrepancies, it should be addressed in future campaigns.

3.3.2 Filter loading and EC-to-TC ratios

Filter overloading with EC can interfere with the optical detection of pyrolytic carbon, potentially leading to a systematically low bias in the reported EC mass concentrations. For aerosols collected at an urban location, Ram et al. (2010) reported that linearity between transmission and EC surface loading was maintained when EC surface loading was kept below 8.0 µg cm^{-2}. Figure S3a presents the observed rBC-to-EC mass ratios as a function of EC surface loading. Several samples collected during the Melpitz winter campaign exceeded the above loading threshold (red shading). However, the rBC-to-EC mass ratio of these data points was very similar to the other filter samples of the Melpitz winter campaigns with lower surface loading. Moreover, no systematic trend exists between surface loading and the rBC-to-EC mass ratio for all other campaigns, where EC surface loading stayed below the above threshold in any case (Table S2). Instead, the bias depends systematically on the campaign as already shown above. Consequently, filter overloading cannot explain the $m_{rBC} - m_{EC-PM2.5}$ discrepancy during the Melpitz winter campaign or for the other campaigns of this study.

The precision of thermal–optical EC mass measurements has been found to degrade at TC surface loadings <10 µg cm^{-2} and at a low EC-to-TC mass ratio (Sect. 2.2.3). Figure S3b presents the observed rBC-to-EC mass ratios as a function of TC surface loading, which frequently dropped to low values of between 2 and 10 µg cm^{-2} during three out of the five campaigns (Table S2). However, this analysis does not suggest increased random noise or systematic bias caused by low TC surface loading (points within red-shaded area). Instead, systematic campaign-dependent bias dominates again.

OC–EC-split-related artifacts in thermal–optical EC mass are more likely to occur at low EC-to-TC mass ratios. Figure S3c presents the observed rBC-to-EC mass ratios as a function of the EC-to-TC mass ratio. No systematic dependence on the EC-to-TC ratio was found, except possibly for the Melpitz winter campaign. However, multiple other aerosol properties exhibited covariance with the EC-to-TC ratio on a campaign-to-campaign basis, as will be addressed in Sect. 3.4. Causality hence remains elusive.

3.3.3 Systematic EC and rBC bias due to the presence of particular types of particulate matter such as brown carbon or biomass burning BC

As discussed in Sect. 2.3.2, the SP2 sensitivity depends on the BC type. Therefore, differences in the BC properties between the atmospheric rBC samples and the calibration material may result in systematic bias. The AAE of an aerosol provides information on brown carbon co-emitted with BC and through this on potential BC sources (Sect. 2.4.2). Figure 5 presents the relation between m_{EC} and m_{rBC}, color-coded by the AAE to investigate a possible influence of the presence of brown carbon. Three zones can be distinguished (see also Table S4 for AAE statistics): the upper part of the figure, with $m_{BC} > 0.3$ µg m^{-3} and $m_{rBC} > m_{EC}$, represents data collected during the winter campaigns of Melpitz and Palaiseau, with an AAE above average (>1.2; blue symbols) and geometric mean AAE values of 1.36 and 1.38, respectively. The lower right part of the figure, with $m_{BC} > 0.3$ µg m^{-3} and $m_{rBC} < m_{EC}$, represents data from Bologna and Cabauw, with $0.8 < \text{AAE} < 1.2$ and geometric mean AAE values of 1.04 (red symbols). The data in the lower left part of the graph, with $m_{BC} < 0.3$ µg m^{-3}, represent Melpitz summer data, with AAEs between 0.93 and 1.28 (upward-pointing triangle markers). While there is a general increase in the relative difference between m_{EC}–m_{rBC} with increasing AAE when considering all campaigns (Fig. S4), it is not explained with the AAE variability within an individual campaign (marked with different colors). Furthermore, tar brown carbon has been shown to be assigned to EC mass (Sect. 2.2.1), while it does not contribute to rBC mass (Sect. 2.3.3). Such tar brown carbon interference would cause a negative relationship of data points as presented in Fig. S4, which was not observed. Hence, the observations do not provide evidence of a substantial fraction of tar brown carbon in total EC in daily averaged samples. We conclude

that the variation in BC sources and carbonaceous aerosol composition, as implied by AAE variability, may contribute to variations in the discrepancy between m_{EC} and m_{rBC}, while not being the main driver of it.

3.4 Reconciliation of sources of discrepancy between rBC and EC mass

The results presented in Fig. 3 and discussed in Sect. 3.2 showed agreement within 8 % between rBC and EC mass concentrations when averaging over all data points from all campaigns. High correlations were found for individual campaigns, however, with large variability in the campaign median rBC-to-EC mass ratios, ranging from 0.53 to 1.29. The analyses presented in Sect. 3.3.3 (Figs. 5 and S4) suggest some relationship between the observed discrepancy and BC source type. However, many aerosol properties related to potential artifacts are cross-correlated, which makes it difficult to identify causal reasons.

The lowest rBC-to-EC mass ratios of 0.53 and 0.65 were observed during the Bologna and Cabauw campaigns (Table 5). The sampled aerosols during these two campaigns were characterized by the smallest BC core sizes, highest EC-to-TC ratios and lowest AAE of ~ 1. The latter shows that BC was dominated by traffic sources. This is the type of ambient aerosol for which the EC mass measurement should be quite reliable (e.g., Khan et al., 2012). The common calibration approach of the SP2 (see Sect. 2.3.2) should only cause limited bias in this case, as it was tailored to match the instrument sensitivity of rBC. Coarse BC particles with sizes between the upper cut-off diameter of the SP2 and the PM inlet cut-off diameter of the EC sampling may contribute to the rBC mass being lower than the EC mass, though the analyses presented in Sect. 3.3.1 did not provide a clear result on the importance of this effect. At the lower end of the BC mass size distribution, rBC mass data were corrected for the missed rBC mass associated with small BC cores (Sects. 2.3.5 and 3.1.1). However, this correction would not account for an additional BC mode below the SP2 cut-off, as hypothesized by, e.g., Liggio et al. (2012) and Cappa et al. (2019), nor could presence of such a mode be excluded by means of particle number-based considerations.

The results for the Melpitz winter campaign are different in many aspects: the highest average rBC-to-EC mass ratio of all campaigns (1.29), largest BC core sizes, highest EC filter loading and highest AAE (Tables S2 and S4). Large artifacts from missed rBC mass below the SP2 LDL could be excluded with number-based considerations (Sect. 3.1.2). The aerosol contained a substantial fraction of coarse BC, based on parallel EC measurements made with PM_1 and $PM_{2.5}$ inlet cut-off diameters. The SP2 might have missed some of these coarse particles. However, this effect likely caused less than a 20 % negative bias in rBC mass concentration, which would have made the discrepancy between rBC and EC mass greater rather than smaller. Based on previous studies (van Pinxteren et al., 2019) and measured AAE, the BC contained substantial contributions from coal burning and/or wood burning emissions. For wood burning BC, this could result in rBC mass that is low by less than ~ 20 % due to potentially lower sensitivity of the SP2 (Laborde et al., 2012a). The sensitivity of the SP2 to BC from coal burning is unknown, but the bias is expected to be <30 %. As for the EC, the analyses presented in Sects. 3.3.2 and 3.3.3 did not provide evidence of a clear bias of the EC mass measurements in one or the other direction.

An agreement within 15 % between rBC and EC mass was observed for the Melpitz summer and Palaiseau campaigns (Table 5), where the pertinent aerosol and BC properties assumed mean values compared to the range covered by data from all campaigns. This finding does not exclude compensating errors in one or both measurements. However, no clear evidence for such errors was observed.

3.5 Comparison with previous rBC and EC intercomparison studies

In this section, we put our results into context with previous rBC and EC mass intercomparison studies available in the literature. Figure 6 contains a compilation of co-located measurements presented as a scatterplot. The data collected in this study are shown with green points; the corresponding median ratio is shown by the green line; and the green area illustrates the 1 GSD range around the geometric mean value. In the same graph, data from previously published ambient, laboratory and chamber studies are reported, including labels indicating the thermal–optical protocol used for the EC measurements. Further information on the data shown in Fig. 6 is given in Table S5 (SP2 calibration material, m_{EC} cut-off, TOA thermal protocol, period, location, site characteristics or aerosol source, and average result of the intercomparison).

The data points of the previous studies are scattered around the 1 : 1 line, and the majority of them lie within the 1 GSD range of this study. Therefore, the previous studies confirm the finding that the TOA and the SP2 techniques both provide a consistent measurement of BC mass within the uncertainties of either technique. More specifically, the chamber experiments with CAST (Combustion Aerosol STandard; Jing Ltd., Switzerland) soot by Laborde et al. (2012b) show agreement between rBC and EC mass within 15 % (topmost cyan point in Fig. 6). Such close agreement is not surprising as the sample comprised almost pure BC, which simplifies the EC mass measurement, and the BC mass size distribution was almost completely within the range covered by the SP2. Corbin et al. (2019) investigated exhaust from a four-stroke ship diesel engine (brown triangles in Fig. 6). Close agreement within a few percent was achieved under engine operation conditions under which the emitted refractory carbon was dominated by soot–BC. By contrast, rBC-to-EC mass ratios substantially smaller than unity were observed when operating the engine under conditions leading

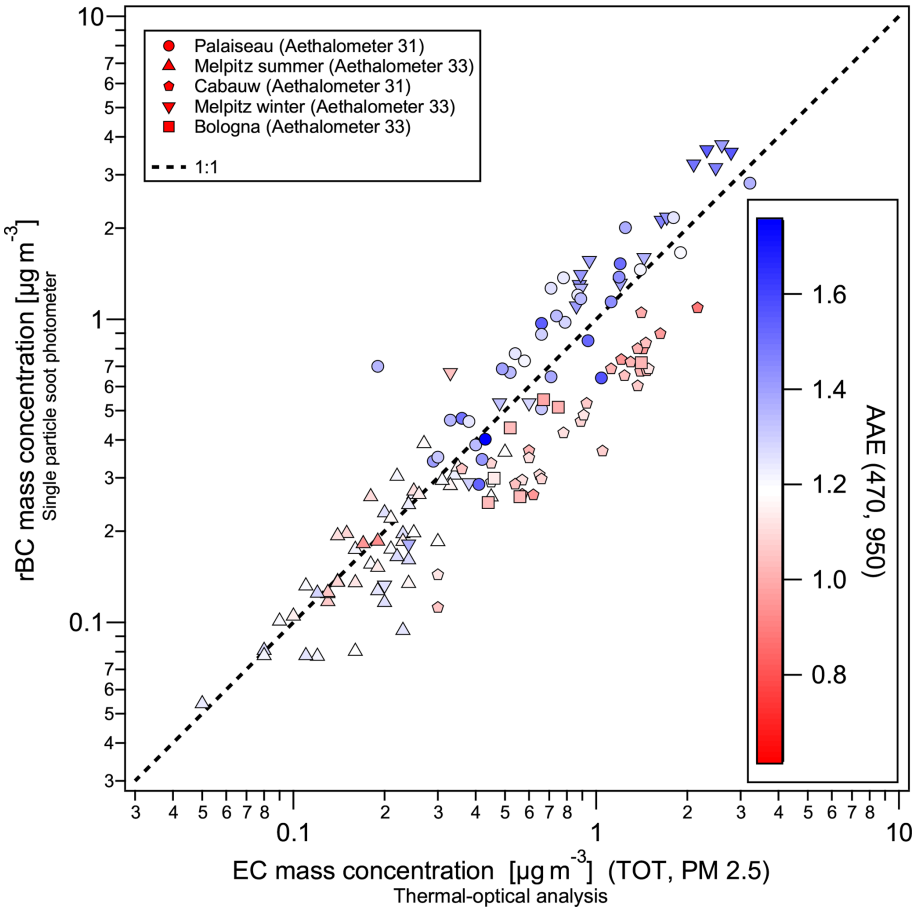

Figure 5. The rBC mass concentration versus EC mass concentration for all campaigns of this study color-coded by the Ångström absorption exponent of each data point.

to a high fraction of tar brown carbon in the exhaust. This discrepancy could be attributed to a positive interference in EC mass caused by tar balls. Miyakawa et al. (2016) measured ambient aerosol at an urban location and found very high correlation and close agreement (within 7 %) between rBC and EC mass (after applying line loss corrections, since they found the particle transmission efficiency of the diffusion dryer of the SP2 line to be 84 %). Zhang et al. (2016) reported an average rBC-to-EC mass ratio of 0.72 for an urban background site, with all data points highly correlated and therefore within the green shading. During the campaign at a remote Arctic site by Sharma et al. (2017), the rBC mass was found to be a factor of 0.51 lower than the EC mass, with half of the data points lying outside the green shading. They attributed this large bias to two potential reasons: first, due to filter loadings being around the limit of quantification of the TOA and, second, due to large charring bias, causing EC mass overestimation despite optical correction. The mean EC mass uncertainty during the campaign was ~ 28 %, reaching values as high as 80 % during summer due to very low EC mass concentrations.

As discussed in Sect. 2.2.3 and shown in Table 1, the difference in the thermal–optical protocols used to quantify m_{EC} can result in a bias of ± 40 %. For example, the geometric mean ratio between rBC and EC mass of the Zhang et al. (2016) data points would increase from 0.72 to 0.96 if they had been measured with the EUSAAR-2 protocol or if the 25 % systematic difference between the IMPROVE and EUSAAR-2 protocols as reported by Han et al. (2016) was applied (see Table 1). However, our campaign-to-campaign variability in the rBC-to-EC mass ratio of roughly ± 50 % using the same TOA protocol, (Fig. 3) can be even bigger than the variability associated with a different TOA protocol for the same sample. Therefore, the rBC mass measured by the SP2 cannot be used to identify the optimal TOA protocol.

4 Conclusions

In this work co-located EC and rBC mass concentration measurements from five field campaigns performed in the time period 2010–2017 across several European sites (Palaiseau, Bologna, Cabauw and Melpitz) were collated and examined

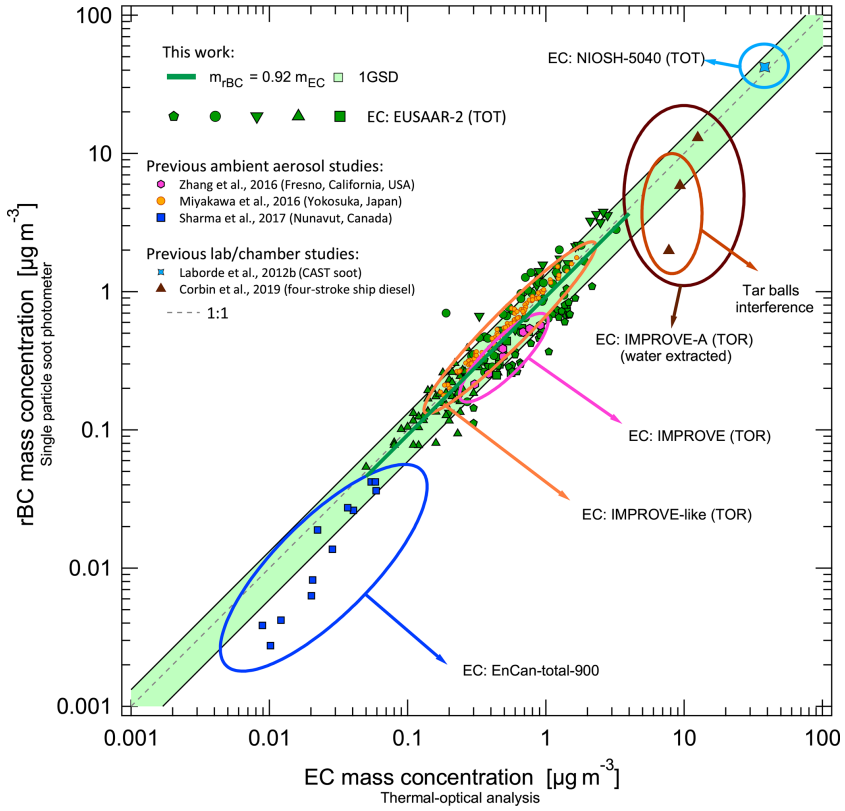

Figure 6. EC mass concentration vs. rBC mass concentration for the datasets studied in this work and other published data.

to identify the differences between BC mass concentrations measured by thermal–optical analysis and the LII technique. All EC concentration measurements were performed with the EUSAAR-2 thermal protocol, with the TOT technique on quartz filters sampled with high volumes with a $PM_{2.5}$ cut-off (except for the Cabauw campaign during which PM_{10} was sampled). All the OC–EC TOA instruments used to perform the EC analysis were compared at the JRC European Reference Laboratory for Air Pollution (ERLAP) to check the EC bias and variability. All rBC mass concentration measurements were performed with SP2 instruments. Three different SP2 instruments (PSI, IGE and AWI) were used in these campaigns, calibrated with the same standard material, fullerene soot, using two different batches, which produced almost identical calibration curves. The mass of BC cores smaller than the lower SP2 detection limit was calculated for all the campaigns including sensitivity analyses. The estimates of missed rBC mass outside the detection range of the SP2 were found to vary between campaigns due to differences in the size distributions of the BC particles.

The observed rBC and EC mass concentrations correlated well with each other. However, the median of the observed rBC-to-EC mass ratios varied from 0.53 to 1.29 from campaign to campaign. Potential reasons for discrepancies are as follows: a source-specific SP2 response, the possible presence of an additional mode of small BC cores below the LDL of the SP2, differences in the upper cut-off of the SP2 and the inlet line for the EC sampling, or various uncertainties and interferences from co-emitted species in the EC mass measurement. The discrepancy between rBC and EC appears to be systematically related to the BC source, i.e., traffic versus wood and/or coal burning. However, it was not possible to identify causalities behind this trend due to potential cross-correlations between several aerosol and BC properties relevant to potential biases. For future intercomparison studies, it is important to constrain the upper cut-off and potential inlet losses of both methods in such a manner that these can be excluded as a source of discrepancy.

The comparison with already published studies showed that most of the rBC-to-EC mass ratio data points of the other campaigns were within 1 GSD of the median and GSD found in this work. Although in this work, all EC concentrations were measured by the EUSAAR-2 protocol, we note that our reported variability in the rBC-to-EC mass ratio is greater than the variability expected between EC concentrations measured by different thermal protocols.

From this study, we conclude that the two methods essentially measure the same quantity; i.e., both provide an operationally defined measure of atmospheric BC mass in good overall agreement. However, systematic discrepancies of up to $\sim \pm 50\,\%$ were observed at some sites. Lack of a traceable reference method or reference aerosols combined with uncer-

tainties in both of the methods made it impossible to clearly quantify the sources of discrepancies or to attribute them to one or the other method.

Data availability. The data archive for this paper is available on Zenodo: https://doi.org/10.5281/zenodo.4445557 (Pileci et al., 2021).

Supplement. The supplement related to this article is available online at: https://doi.org/10.5194/amt-14-1379-2021-supplement.

Author contributions. REP, MB and RLM took the rBC measurements and/or analyzed the raw data during the Bologna campaign. AT was responsible for the EC measurements during the Bologna campaign. AM coordinated the Bologna campaign. JY, MZ and RLM took the measurements and/or analyzed the raw data during the Melpitz winter campaign while JCC took the measurements and analyzed the raw data during the Melpitz summer campaign. TT, TM and BW took the data and coordinated the Melpitz campaigns. GS was responsible for the EC measurements during the Melpitz campaigns. BH, MMM and RLM were responsible for coordination and/or measurements during the Cabauw campaign. JPP performed calibrations of the thermal–optical OC–EC analyzers. REP synthesized all data sets, interpreted the results and wrote the manuscript together with RLM and MGB. All co-authors reviewed and commented on the manuscript.

Competing interests. The authors declare that they have no conflict of interest.

Disclaimer. The opinions expressed and arguments employed herein do not necessarily reflect the official views of the Swiss Government.

Acknowledgements. The authors are grateful to Achim Grüner for the technical support during the two Melpitz campaigns. We also thank Claudia Zigola (ARPAE) who performed the TOA of the filters during the Bologna campaign. The logistic support of CNR-ISAC technical staff (Francescopiero Calzolari) during the Bologna campaign is appreciated. Many thanks go to the technical support of Günther Wehrle during the Bologna campaign.

Financial support. This work received financial support from the ERC (grant ERC-CoG-615922-BLACARAT) and from the ACTRIS-2 project (EU H2020-INFRAIA-2014-2015, grant agreement no. 654109, and Swiss State Secretariat for Education, Research and Innovation, contract number 15.0159-1). In addition, the field campaigns were supported by the Transnational Access scheme of the ACTRIS-2 project. MZ received financial support from the Deutsche Forschungsgemeinschaft (DFG, German Research Foundation) – Projektnummer 268020496 – TRR 172, within the Transregional Collaborative Research Centre "ArctiC Amplification: Climate Relevant Atmospheric and SurfaCe Processes and Feedback Mechanisms $(AC)^3$".

Review statement. This paper was edited by Pierre Herckes and reviewed by two anonymous referees.

References

Aakko-Saksa, P., Koponen, P., Aurela, M., Vesala, H., Piimäkorpi, P., Murtonen, T., Sippula, O., Koponen, H., Karjalainen, P., Kuittinen, N., Panteliadis, P., Rönkkö, T., and Timonen, H.: Considerations in analysing elemental carbon from marine engine exhaust using residual, distillate and biofuels, J. Aerosol Sci., 126, 191–204, https://doi.org/10.1016/j.jaerosci.2018.09.005, 2018.

Adachi, K., Chung, S. H., and Buseck, P. R.: Shapes of soot aerosol particles and implications for their effects on climate, J. Geophys. Res., 115, D15206, https://doi.org/10.1029/2009JD012868, 2010.

Adachi, K., Sedlacek, A. J., Kleinman, L., Springston, S. R., Wang, J., Chand, D., Hubbe, J. M., Shilling, J. E., Onasch, T. B., Kinase, T., Sakata, K., Takahashi, Y., and Buseck, P. R.: Spherical tarball particles form through rapid chemical and physical changes of organic matter in biomass-burning smoke, P. Natl. Acad. Sci. USA, 116, 19336–19341, https://doi.org/10.1073/pnas.1900129116, 2019.

Altstädter, B., Platis, A., Jähn, M., Baars, H., Lückerath, J., Held, A., Lampert, A., Bange, J., Hermann, M., and Wehner, B.: Airborne observations of newly formed boundary layer aerosol particles under cloudy conditions, Atmos. Chem. Phys., 18, 8249–8264, https://doi.org/10.5194/acp-18-8249-2018, 2018.

Arnott, W. P., Moosmüller, H., Sheridan, P. J., Ogren, J. A., Raspet, R., Slaton, W. V., Hand, J. L., Kreidenweis, S. M., and Collett Jr., J. L.: Photoacoustic and filter-based ambient aerosol light absorption measurements: Instrument comparisons and the role of relative humidity, J. Geophys. Res.-Atmos., 108, 4034, https://doi.org/10.1029/2002JD002165, 2003.

Baumgardner, D., Popovicheva, O., Allan, J., Bernardoni, V., Cao, J., Cavalli, F., Cozic, J., Diapouli, E., Eleftheriadis, K., Genberg, P. J., Gonzalez, C., Gysel, M., John, A., Kirchstetter, T. W., Kuhlbusch, T. A. J., Laborde, M., Lack, D., Müller, T., Niessner, R., Petzold, A., Piazzalunga, A., Putaud, J. P., Schwarz, J., Sheridan, P., Subramanian, R., Swietlicki, E., Valli, G., Vecchi, R., and Viana, M.: Soot reference materials for instrument calibration and intercomparisons: a workshop summary with recommendations, Atmos. Meas. Tech., 5, 1869–1887, https://doi.org/10.5194/amt-5-1869-2012, 2012.

Bautista, A. T., Pabroa, P. C. B., Santos, F. L., Quirit, L. L., Asis, J. L. B., Dy, M. A. K., and Martinez, J. P. G.: Intercomparison between NIOSH, IMPROVE_A, and EUSAAR_2 protocols: Finding an optimal thermal–optical protocol for Philippines OC/EC samples, Atmos. Pollut. Res., 6, 334–342, https://doi.org/10.5094/APR.2015.037, 2015.

Birch, M., Dahmann, D., and Fricke, H.-H.: Comparison of two carbon analysis methods for monitoring diesel particulate levels in mines, J. Environ. Monit., 1, 541–544, https://doi.org/10.1039/A905204F, 1999.

Birch, M. E. and Cary, R. A.: Elemental carbon-based method for monitoring occupational exposures to particulate diesel exhaust, Aerosol Sci. Technol., 25, 221–241, https://doi.org/10.1080/02786829608965393, 1996.

Bond, T. C.: Spectral dependence of visible light absorption by carbonaceous particles emitted from coal combustion, Geophys. Res. Lett., 28, 4075–4078, https://doi.org/10.1029/2001GL013652, 2001.

Bond, T. C. and Bergström, R. W.: Light absorption by carbonaceous particles: An investigative review, Aerosol Sci. Technol., 40, 27–67, https://doi.org/10.1080/02786820500421521, 2006.

Bond, T. C., Doherty, S. J., Fahey, D. W., Forster, P. M., Berntsen, T., DeAngelo, B. J., Flanner, M. G., Ghan, S., Kärcher, B., Koch, D., Kinne, S., Kondo, Y., Quinn, P. K., Sarofim, M. C., Schultz, M. G., Schulz, M., Venkataraman, C., Zhang, H., Zhang, S., Bellouin, N., Guttikunda, S. K., Hopke, P. K., Jacobson, M. Z., Kaiser, J. W., Klimont, Z., Lohmann, U., Schwarz, J. P., Shindell, D., Storelvmo, T., Warren, S. G., and Zender, C. S.: Bounding the role of black carbon in the climate system: A scientific assessment, J. Geophys. Res.-Atmos., 118, 5380–5552, https://doi.org/10.1002/jgrd.50171, 2013.

Bucci, S., Cristofanelli, P., Decesari, S., Marinoni, A., Sandrini, S., Größ, J., Wiedensohler, A., Di Marco, C. F., Nemitz, E., Cairo, F., Di Liberto, L., and Fierli, F.: Vertical distribution of aerosol optical properties in the Po Valley during the 2012 summer campaigns, Atmos. Chem. Phys., 18, 5371–5389, https://doi.org/10.5194/acp-18-5371-2018, 2018.

Burtscher, H., Baltensperger, U., Bukowiecki, N., Cohn, P., Hüglin, C., Mohr, M., Matter, U., Nyeki, S., Schmatloch, V., Streit, N., and Weingartner, E.: Separation of volatile and non-volatile aerosol fractions by thermodesorption: instrumental development and applications, J. Aerosol Sci., 32, 427–442, https://doi.org/10.1016/S0021-8502(00)00089-6, 2001.

Cappa, C. D., Zhang, X., Russell, L. M., Collier, S., Lee, A. K. Y., Chen, C.-L., Betha, R., Chen, S., Liu, J., Price, D. J., Sanchez, K. J., McMeeking, G. R., Williams, L. R., Onasch, T. B., Worsnop, D. R., Abbatt, J., and Zhang, Q.: Light absorption by ambient black and brown carbon and its dependence on black carbon coating state for two California, USA, cities in winter and summer, J. Geophys. Res.-Atmos., 124, 1550–1577, https://doi.org/10.1029/2018JD029501, 2019.

Cavalli, F., Viana, M., Yttri, K. E., Genberg, J., and Putaud, J.-P.: Toward a standardised thermal-optical protocol for measuring atmospheric organic and elemental carbon: the EUSAAR protocol, Atmos. Meas. Tech., 3, 79–89, https://doi.org/10.5194/amt-3-79-2010, 2010.

Chan, T. W., Huang, L., Leaitch, W. R., Sharma, S., Brook, J. R., Slowik, J. G., Abbatt, J. P. D., Brickell, P. C., Liggio, J., Li, S.-M., and Moosmüller, H.: Observations of OM/OC and specific attenuation coefficients (SAC) in ambient fine PM at a rural site in central Ontario, Canada, Atmos. Chem. Phys., 10, 2393–2411, https://doi.org/10.5194/acp-10-2393-2010, 2010.

Chen, L.-W. A., Chow, J. C., Wang, X. L., Robles, J. A., Sumlin, B. J., Lowenthal, D. H., Zimmermann, R., and Watson, J. G.: Multi-wavelength optical measurement to enhance thermal/optical analysis for carbonaceous aerosol, Atmos. Meas. Tech., 8, 451–461, https://doi.org/10.5194/amt-8-451-2015, 2015.

Cheng, Y., He, K.-B., Duan, F.-K., Du, Z.-Y., Zheng, M., and Ma, Y.-L.: Ambient organic carbon to elemental carbon ratios: Influence of the thermal-optical temperature protocol and implications, Sci. Total Environ., 468–469, 1103–1111, https://doi.org/10.1016/j.scitotenv.2013.08.084, 2013.

Cheung, H. H. Y., Tan, H., Xu, H., Li, F., Wu, C., Yu, J. Z., and Chan, C. K.: Measurements of non-volatile aerosols with a VTDMA and their correlations with carbonaceous aerosols in Guangzhou, China, Atmos. Chem. Phys., 16, 8431–8446, https://doi.org/10.5194/acp-16-8431-2016, 2016.

Chiappini, L., Verlhac, S., Aujay, R., Maenhaut, W., Putaud, J. P., Sciare, J., Jaffrezo, J. L., Liousse, C., Galy-Lacaux, C., Alleman, L. Y., Panteliadis, P., Leoz, E., and Favez, O.: Clues for a standardised thermal-optical protocol for the assessment of organic and elemental carbon within ambient air particulate matter, Atmos. Meas. Tech., 7, 1649–1661, https://doi.org/10.5194/amt-7-1649-2014, 2014.

Chow, J. C., Watson, J. G., Pritchett, L. C., Pierson, W. R., Frazier, C. A., and Purcell, R. G.: The dri thermal/optical reflectance carbon analysis system: description, evaluation and applications in U.S. Air quality studies, Atmos. Environ., 27, 1185–1201, https://doi.org/10.1016/0960-1686(93)90245-T, 1993.

Chow, J. C., Watson, J. G., Crow, D., Lowenthal, D. H., and Merrifield, T.: Comparison of IMPROVE and NIOSH carbon measurements, Aerosol Sci. Technol., 34, 23–34, https://doi.org/10.1080/02786820119073, 2001.

Chow, J. C., Watson, J. G., Chen, L.-W. A., Arnott, W. P., Moosmüller, H., and Fung, K.: Equivalence of elemental carbon by thermal/optical reflectance and transmittance with different temperature protocols, Environ. Sci. Technol., 38, 4414–4422, https://doi.org/10.1021/es034936u, 2004.

Chow, J. C., Watson, J. G., Chen, L.-W. A., Chang, M. C. O., Robinson, N. F., Trimble, D., and Kohl, S.: The IMPROVE_A temperature protocol for thermal/optical carbon analysis: maintaining consistency with a long-term database, J. Air Waste Manag. Assoc., 57, 1014–1023, https://doi.org/10.3155/1047-3289.57.9.1014, 2007.

Clarke, A. D., Shinozuka, Y., Kapustin, V. N., Howell, S., Huebert, B., Doherty, S., Anderson, T., Covert, D., Anderson, J., Hua, X., Moore II, K. G., McNaughton, C., Carmichael, G., and Weber, R.: Size distributions and mixtures of dust and black carbon aerosol in Asian outflow: Physiochemistry and optical properties, J. Geophys. Res.-Atmos., 109, S1217–S1218, https://doi.org/10.1029/2003JD004378, 2004.

Corbin, J. C. and Gysel-Beer, M.: Detection of tar brown carbon with a single particle soot photometer (SP2), Atmos. Chem. Phys., 19, 15673–15690, https://doi.org/10.5194/acp-19-15673-2019, 2019.

Corbin, J. C., Sierau, B., Gysel, M., Laborde, M., Keller, A., Kim, J., Petzold, A., Onasch, T. B., Lohmann, U., and Mensah, A. A.: Mass spectrometry of refractory black carbon particles from six sources: carbon-cluster and oxygenated ions, Atmos. Chem. Phys., 14, 2591–2603, https://doi.org/10.5194/acp-14-2591-2014, 2014.

Corbin, J. C., Lohmann, U., Sierau, B., Keller, A., Burtscher, H., and Mensah, A. A.: Black carbon surface oxidation and organic composition of beech-wood soot aerosols, Atmos. Chem. Phys., 15, 11885–11907, https://doi.org/10.5194/acp-15-11885-2015, 2015.

Corbin, J. C., Pieber, S. M., Czech, H., Zanatta, M., Jakobi, G., Massabò, D., Orasche, J., El Haddad, I., Mensah, A.

A., Stengel, B., Drinovec, L., Mocnik, G., Zimmermann, R., Prévôt, A. S. H., and Gysel, M.: Brown and black carbon emitted by a marine engine operated on heavy fuel oil and distillate fuels: optical properties, size distributions, and emission factors, J. Geophys. Res-Atmos., 123, 6175–6195, https://doi.org/10.1029/2017JD027818, 2018.

Corbin, J. C., Czech, H., Massabò, D., de Mongeot, F. B., Jakobi, G., Liu, F., Lobo, P., Mennucci, C., Mensah, A. A., Orasche, J., Pieber, S. M., Prévôt, A. S. H., Stengel, B., Tay, L.-L., Zanatta, M., Zimmermann, R., El Haddad, I., and Gysel, M.: Infrared-absorbing carbonaceous tar can dominate light absorption by marine-engine exhaust, NPJ Clim. Atmos. Sci., 2, 12, https://doi.org/10.1038/s41612-019-0069-5, 2019.

Corbin, J. C., Moallemi, A., Liu, F., Gagné, S., Olfert, J. S., Smallwood, G. J., and Lobo, P.: Closure between particulate matter concentrations measured ex situ by thermal–optical analysis and in situ by the CPMA–electrometer reference mass system, Aerosol Sci. Technol., 54, 1293–1309, https://doi.org/10.1080/02786826.2020.1788710, 2020.

Drinovec, L., Močnik, G., Zotter, P., Prévôt, A. S. H., Ruckstuhl, C., Coz, E., Rupakheti, M., Sciare, J., Müller, T., Wiedensohler, A., and Hansen, A. D. A.: The "dual-spot" Aethalometer: an improved measurement of aerosol black carbon with real-time loading compensation, Atmos. Meas. Tech., 8, 1965–1979, https://doi.org/10.5194/amt-8-1965-2015, 2015.

Durdina, L., Brem, B. T., Setyan, A., Siegerist, F., Rindlisbacher, T., and Wang, J.: Assessment of particle pollution from jetliners: From smoke visibility to nanoparticle counting, Environ. Sci. Technol., 51, 3534–3541, https://doi.org/10.1021/acs.est.6b05801, 2017.

Durdina, L., Brem, B. T., Schönenberger, D., Siegerist, F., Anet, J. G., and Rindlisbacher, T.: Nonvolatile particulate matter emissions of a business jet measured at ground level and estimated for cruising altitudes, Environ. Sci. Technol., 53, 12865–12872, https://doi.org/10.1021/acs.est.9b02513, 2019.

European Committee for Standardization: Ambient air – Measurement of elemental carbon (EC) and organic carbon (OC) collected on filters: EN 16909:2017, available at: https://standards.cen.eu/dyn/www/f?p=204:110:0::::FSP_PROJECT,FSP_ORG_ID:39908,6245&cs=10D493A2AD690A6AB4340BE3D316277CA (last access: 18 February 2021), 2017.

Fung, K.: Particulate carbon speciation by MnO_2 oxidation, Aerosol Sci. Technol., 12, 122–127, https://doi.org/10.1080/02786829008959332, 1990.

Giannoni, M., Calzolai, G., Chiari, M., Cincinelli, A., Lucarelli, F., Martellini, T., and Nava, S.: A comparison between thermal-optical transmittance elemental carbon measured by different protocols in PM2.5 samples, Sci. Total Environ., 571, 195–205, https://doi.org/10.1016/j.scitotenv.2016.07.128, 2016.

Grahame, T. J., Klemm, R., and Schlesinger, R. B.: Public health and components of particulate matter: The changing assessment of black carbon, J. Air Waste Manag. Assoc., 64, 620–660, https://doi.org/10.1080/10962247.2014.912692, 2014.

Gysel, M., Laborde, M., Olfert, J. S., Subramanian, R., and Gröhn, A. J.: Effective density of Aquadag and fullerene soot black carbon reference materials used for SP2 calibration, Atmos. Meas. Tech., 4, 2851–2858, https://doi.org/10.5194/amt-4-2851-2011, 2011.

Gysel, M., Laborde, M., Mensah, A. A., Corbin, J. C., Keller, A., Kim, J., Petzold, A., and Sierau, B.: Technical Note: The single particle soot photometer fails to reliably detect PALAS soot nanoparticles, Atmos. Meas. Tech., 5, 3099–3107, https://doi.org/10.5194/amt-5-3099-2012, 2012.

Haeffelin, M., Barthès, L., Bock, O., Boitel, C., Bony, S., Bouniol, D., Chepfer, H., Chiriaco, M., Cuesta, J., Delanoë, J., Drobinski, P., Dufresne, J.-L., Flamant, C., Grall, M., Hodzic, A., Hourdin, F., Lapouge, F., Lemaître, Y., Mathieu, A., Morille, Y., Naud, C., Noël, V., O'Hirok, W., Pelon, J., Pietras, C., Protat, A., Romand, B., Scialom, G., and Vautard, R.: SIRTA, a ground-based atmospheric observatory for cloud and aerosol research, Ann. Geophys., 23, 253–275, https://doi.org/10.5194/angeo-23-253-2005, 2005.

Han, Y. M., Chen, L.-W. A., Huang, R.-J., Chow, J. C., Watson, J. G., Ni, H. Y., Liu, S. X., Fung, K. K., Shen, Z. X., Wei, C., Wang, Q. Y., Tian, J., Zhao, Z. Z., Prévôt, A. S. H., and Cao, J. J.: Carbonaceous aerosols in megacity Xi'an, China: Implications of thermal/optical protocols comparison, Atmos. Environ., 132, 58–68, https://doi.org/10.1016/j.atmosenv.2016.02.023, 2016.

Hansen, A. D. A., Rosen, H., and Novakov, T.: The aethalometer – An instrument for the real-time measurement of optical absorption by aerosol particles, Sci. Total Environ., 36, 191–196, https://doi.org/10.1016/0048-9697(84)90265-1, 1984.

Hitzenberger, R., Petzold, A., Bauer, H., Ctyroky, P., Pouresmaeil, P., Laskus, L., and Puxbaum, H.: Intercomparison of thermal and optical measurement methods for elemental carbon and black carbon at an urban location, Environ. Sci. Technol., 40, 6377–6383, https://doi.org/10.1021/es051228v, 2006.

Hodnebrog, Ø., Myhre, G., and Samset, B. H.: How shorter black carbon lifetime alters its climate effect, Nat. Commun., 5, 5065, https://doi.org/10.1038/ncomms6065, 2014.

Huang, L., Brook, J. R., Zhang, W., Li, S. M., Graham, L., Ernst, D., Chivulescu, A., and Lu, G.: Stable isotope measurements of carbon fractions (OC/EC) in airborne particulate: A new dimension for source characterization and apportionment, Atmos. Environ., 40, 2690–2705, https://doi.org/10.1016/j.atmosenv.2005.11.062, 2006.

Huntzicker, J. J., Johnson, R. L., Shah, J. J., and Cary, R. A.: Analysis of organic and elemental carbon in ambient aerosols by a thermal-optical method, in: Particulate Carbon: Atmospheric Life Cycle, edited: by Wolff, G. T. and Klimisch, R. L., Springer US, Boston, MA, 79–88, 1982.

Karanasiou, A., Diapouli, E., Cavalli, F., Eleftheriadis, K., Viana, M., Alastuey, A., Querol, X., and Reche, C.: On the quantification of atmospheric carbonate carbon by thermal/optical analysis protocols, Atmos. Meas. Tech., 4, 2409–2419, https://doi.org/10.5194/amt-4-2409-2011, 2011.

Karanasiou, A., Minguillón, M. C., Viana, M., Alastuey, A., Putaud, J.-P., Maenhaut, W., Panteliadis, P., Močnik, G., Favez, O., and Kuhlbusch, T. A. J.: Thermal-optical analysis for the measurement of elemental carbon (EC) and organic carbon (OC) in ambient air a literature review, Atmos. Meas. Tech. Discuss., 8, 9649–9712, https://doi.org/10.5194/amtd-8-9649-2015, 2015.

Khan, B., Hays, M. D., Geron, C., and Jetter, J.: Differences in the OC/EC ratios that characterize ambient and source aerosols due to thermal-optical analysis, Aerosol Sci. Technol., 46, 127–137, https://doi.org/10.1080/02786826.2011.609194, 2012.

Kirchstetter, T. W., Novakov, T., and Hobbs P. V.: Evidence that the spectral dependence of light absorption by aerosols is affected by organic carbon, J. Geophys. Res.-Atmos., 109, D21208, https://doi.org/10.1029/2004JD004999, 2004.

Kupiszewski, P., Zanatta, M., Mertes, S., Vochezer, P., Lloyd, G., Schneider, J., Schenk, L., Schnaiter, M., Baltensperger, U., Weingartner, E. and Gysel, M.: Ice residual properties in mixed-phase clouds at the high-alpine Jungfraujoch site, J. Geophys. Res.-Atmos., 121, 12343–12362, https://doi.org/10.1002/2016JD024894, 2016.

Laborde, M., Mertes, P., Zieger, P., Dommen, J., Baltensperger, U., and Gysel, M.: Sensitivity of the Single Particle Soot Photometer to different black carbon types, Atmos. Meas. Tech., 5, 1031–1043, https://doi.org/10.5194/amt-5-1031-2012, 2012a.

Laborde, M., Schnaiter, M., Linke, C., Saathoff, H., Naumann, K.-H., Möhler, O., Berlenz, S., Wagner, U., Taylor, J. W., Liu, D., Flynn, M., Allan, J. D., Coe, H., Heimerl, K., Dahlkötter, F., Weinzierl, B., Wollny, A. G., Zanatta, M., Cozic, J., Laj, P., Hitzenberger, R., Schwarz, J. P., and Gysel, M.: Single Particle Soot Photometer intercomparison at the AIDA chamber, Atmos. Meas. Tech., 5, 3077–3097, https://doi.org/10.5194/amt-5-3077-2012, 2012b.

Laborde, M., Crippa, M., Tritscher, T., Jurányi, Z., Decarlo, P. F., Temime-Roussel, B., Marchand, N., Eckhardt, S., Stohl, A., Baltensperger, U., Prévôt, A. S. H., Weingartner, E., and Gysel, M.: Black carbon physical properties and mixing state in the European megacity Paris, Atmos. Chem. Phys., 13, 5831–5856, https://doi.org/10.5194/acp-13-5831-2013, 2013.

Liggio, J., Gordon, M., Smallwood, G., Li, S.-M., Stroud, C., Staebler, R., Lu, G., Lee, P., Taylor, B., and Brook, J. R.: Are emissions of black carbon from gasoline vehicles underestimated? Insights from near and on-road measurements, Environ. Sci. Technol., 46, 4819–4828, https://doi.org/10.1021/es2033845, 2012.

Liu, D., Allan, J. D., Young, D. E., Coe, H., Beddows, D., Fleming, Z. L., Flynn, M. J., Gallagher, M. W., Harrison, R. M., Lee, J., Prevot, A. S. H., Taylor, J. W., Yin, J., Williams, P. I., and Zotter, P.: Size distribution, mixing state and source apportionment of black carbon aerosol in London during wintertime, Atmos. Chem. Phys., 14, 10061–10084, https://doi.org/10.5194/acp-14-10061-2014, 2014.

Lobo, P., Durdina, L., Smallwood, G. J., Rindlisbacher, T., Siegerist, F., Black, E. A., Yu, Z., Mensah, A. A., Hagen, D. E., Miake-Lye, R. C., Thomson, K. A., Brem, B. T., Corbin, J. C., Abegglen, M., Sierau, B., Whitefield, P. D., and Wang, J.: Measurement of aircraft engine non-volatile PM emissions: Results of the aviation-particle regulatory instrumentation demonstration experiment (A-PRIDE) 4 campaign, Aerosol Sci. Technol., 49, 472–484, https://doi.org/10.1080/02786826.2015.1047012, 2015.

Massabò, D., Altomari, A., Vernocchi, V., and Prati, P.: Two-wavelength thermal–optical determination of light-absorbing carbon in atmospheric aerosols, Atmos. Meas. Tech., 12, 3173–3182, https://doi.org/10.5194/amt-12-3173-2019, 2019.

Matsui, H., Hamilton, D. S., and Mahowald, N. M.: Black carbon radiative effects highly sensitive to emitted particle size when resolving mixing-state diversity, Nat. Commun., 9, 3446, https://doi.org/10.1038/s41467-018-05635-1, 2018.

Medalia, A. I. and Heckman, F. A.: Morphology of aggregates—II. Size and shape factors of carbon black aggregates from electron microscopy, Carbon, 7, 567–582, https://doi.org/10.1016/0008-6223(69)90029-3, 1969.

Michelsen, H. A., Schulz, C., Smallwood, G. J., and Will, S.: Laser-induced incandescence: Particulate diagnostics for combustion, atmospheric, and industrial applications, Prog. Energy Combust. Sci., 51, 2–48, https://doi.org/10.1016/j.pecs.2015.07.001, 2015.

Miyakawa, T., Kanaya, Y., Komazaki, Y., Taketani, F., Pan, X., Irwin, M., and Symonds, J.: Intercomparison between a single particle soot photometer and evolved gas analysis in an industrial area in Japan: Implications for the consistency of soot aerosol mass concentration measurements, Atmos. Environ., 127, 14–21, https://doi.org/10.1016/j.atmosenv.2015.12.018, 2016.

Momenimovahed, A. and Olfert, J. S.: Effective density and volatility of particles emitted from gasoline direct injection vehicles and implications for particle mass measurement, Aerosol Sci. Technol., 49, 1051–1062, https://doi.org/10.1080/02786826.2015.1094181, 2015.

Moosmüller, H., Chakrabarty, R. K., and Arnott, W. P.: Aerosol light absorption and its measurement: A review, J. Quant. Spectrosc. Ra., 110, 844–878, https://doi.org/10.1016/j.jqsrt.2009.02.035, 2009.

Moteki, N. and Kondo, Y.: Effects of mixing state on black carbon measurements by laser-induced incandescence, Aerosol Sci. Technol., 41, 398–417, https://doi.org/10.1080/02786820701199728, 2007.

Moteki, N. and Kondo, Y.: Dependence of laser-induced incandescence on physical properties of black carbon aerosols: Measurements and theoretical interpretation, Aerosol Sci. Technol., 44, 663–675, https://doi.org/10.1080/02786826.2010.484450, 2010.

Moteki, N., Adachi, K., Ohata, S., Yoshida, A., Harigaya, T., Koike, M., and Kondo, Y.: Anthropogenic iron oxide aerosols enhance atmospheric heating, Nat. Commun., 8, 15329, https://doi.org/10.1038/ncomms15329, 2017.

Petit, J.-E., Favez, O., Sciare, J., Crenn, V., Sarda-Estève, R., Bonnaire, N., Močnik, G., Dupont, J.-C., Haeffelin, M., and Leoz-Garziandia, E.: Two years of near real-time chemical composition of submicron aerosols in the region of Paris using an Aerosol Chemical Speciation Monitor (ACSM) and a multi-wavelength Aethalometer, Atmos. Chem. Phys., 15, 2985–3005, https://doi.org/10.5194/acp-15-2985-2015, 2015.

Petzold, A., Schloesser, H., Sheridan, P. J., Arnott, W. P., Ogren, J. A., and Virkkula, A.: Evaluation of multiangle absorption photometry for measuring aerosol light absorption, Aerosol Sci. Technol., 39, 40–51, https://doi.org/10.1080/027868290901945, 2005.

Petzold, A., Ogren, J. A., Fiebig, M., Laj, P., Li, S.-M., Baltensperger, U., Holzer-Popp, T., Kinne, S., Pappalardo, G., Sugimoto, N., Wehrli, C., Wiedensohler, A., and Zhang, X.-Y.: Recommendations for reporting "black carbon" measurements, Atmos. Chem. Phys., 13, 8365–8379, https://doi.org/10.5194/acp-13-8365-2013, 2013.

Piazzalunga, A., Bernardoni, V., Fermo, P., Valli, G., and Vecchi, R.: Technical Note: On the effect of water-soluble compounds removal on EC quantification by TOT analysis in urban aerosol samples, Atmos. Chem. Phys., 11, 10193–10203, https://doi.org/10.5194/acp-11-10193-2011, 2011.

Pileci, R. E., Modini, R. L., Berò, M., Yuan, J., Corbin, J. C., Marinoni, A., Henzing, B. J., Moerman, M. M., Putaud, J. P., Spindler, G., Wehner, B., Müller, T., Tuch, T., Tren-

tini, A., Zanatta, M., Baltensperger, U., and Gysel-Beer, M.: Data archive for the journal article: "Comparison of co-located rBC and EC mass concentration measurements during field campaigns at several European sites", Data set, Zenodo, https://doi.org/10.5281/zenodo.4445557, 2021.

Putaud, J.-P., Van Dingenen, R., Alastuey, A., Bauer, H., Birmili, W., Cyrys, J., Flentje, H., Fuzzi, S., Gehrig, R., Hansson, H. C., Harrison, R. M., Herrmann, H., Hitzenberger, R., Hüglin, C., Jones, A. M., Kasper-Giebl, A., Kiss, G., Kousa, A., Kuhlbusch, T. A. J., Löschau, G., Maenhaut, W., Molnar, A., Moreno, T., Pekkanen, J., Perrino, C., Pitz, M., Puxbaum, H., Querol, X., Rodriguez, S., Salma, I., Schwarz, J., Smolik, J., Schneider, J., Spindler, G., ten Brink, H., Tursic, J., Viana, M., Wiedensohler, A., and Raes, F.: A European aerosol phenomenology – 3: Physical and chemical characteristics of particulate matter from 60 rural, urban, and kerbside sites across Europe, Atmos. Environ., 44, 1308–1320, https://doi.org/10.1016/j.atmosenv.2009.12.011, 2010.

Querol, X., Moreno, T., Karanasiou, A., Reche, C., Alastuey, A., Viana, M., Font, O., Gil, J., de Miguel, E., and Capdevila, M.: Variability of levels and composition of PM_{10} and $PM_{2.5}$ in the Barcelona metro system, Atmos. Chem. Phys., 12, 5055–5076, https://doi.org/10.5194/acp-12-5055-2012, 2012.

Ram, K., Sarin, M. M., and Tripathi, S. N.: Inter-comparison of thermal and optical methods for determination of atmospheric black carbon and attenuation coefficient from an urban location in northern India, Atmos. Res., 97, 335–342, https://doi.org/10.1016/j.atmosres.2010.04.006, 2010.

Reddington, C. L., McMeeking, G., Mann, G. W., Coe, H., Frontoso, M. G., Liu, D., Flynn, M., Spracklen, D. V., and Carslaw, K. S.: The mass and number size distributions of black carbon aerosol over Europe, Atmos. Chem. Phys., 13, 4917–4939, https://doi.org/10.5194/acp-13-4917-2013, 2013.

Reisinger, P., Wonaschütz, A., Hitzenberger, R., Petzold, A., Bauer, H., Jankowski, N., Puxbaum, H., Chi, X., and Maenhaut, W.: Intercomparison of measurement techniques for black or elemental carbon under urban background conditions in wintertime: Influence of biomass combustion, Environ. Sci. Technol., 42, 884–889, https://doi.org/10.1021/es0715041, 2008.

Ricciardelli, I., Bacco, D., Rinaldi, M., Bonafè, G., Scotto, F., Trentini, A., Bertacci, G., Ugolini, P., Zigola, C., Rovere, F., Maccone, C., Pironi, C., and Poluzzi, V.: A three-year investigation of daily PM2.5 main chemical components in four sites: The routine measurement program of the Supersito Project (Po Valley, Italy), Atmos. Environ., 152, 418–430, https://doi.org/10.1016/j.atmosenv.2016.12.052, 2017.

Rosen, H., Hansen, A. D. A., Gundel, L., and Novakov, T.: Identification of the optically absorbing component in urban aerosols, Appl. Opt., 17, 3859–3861, https://doi.org/10.1364/AO.17.003859, 1978.

Saleh, R., Cheng, Z., and Atwi, K.: The Brown–Black Continuum of Light-Absorbing Combustion Aerosols, Environ. Sci. Technol. Lett., 5, 508–513, https://doi.org/10.1021/acs.estlett.8b00305, 2018.

Samset, B. H., Stjern, C. W., Andrews, E., Kahn, R. A., Myhre, G., Schulz, M., and Schuster, G. L.: Aerosol absorption: Progress towards global and regional constraints, Curr. Clim. Change Rep., 4, 65–83, https://doi.org/10.1007/s40641-018-0091-4, 2018.

Schraml, S., Heimgärtner, C., Will, S., Leipertz, A., and Hemm, A.: Application of a New Soot Sensor for Exhaust Emission Control Based on Time Resolved Laser Induced Incandescence (TIRE-LII), SAE Transactions, 109, 2629–2638, 2000.

Schwarz, J. P.: Extrapolation of single particle soot photometer incandescent signal data, Aerosol Sci. Technol., 53, 911–920, https://doi.org/10.1080/02786826.2019.1610154, 2019.

Schwarz, J. P., Gao, R. S., Fahey, D. W., Thomson, D. S., Watts, L. A., Wilson, J. C., Reeves, J. M., Darbeheshti, M., Baumgardner, D. G., Kok, G. L., Chung, S. H., Schulz, M., Hendricks, J., Lauer, A., Kärcher, B., Slowik, J. G., Rosenlof, K. H., Thompson, T. L., Langford, A. O., Loewenstein, M. and Aikin, K. C.: Single-particle measurements of midlatitude black carbon and light-scattering aerosols from the boundary layer to the lower stratosphere, J. Geophys. Res.-Atmos., 111, https://doi.org/10.1029/2006JD007076, 2006.

Schwarz, J. P., Spackman, J. R., Gao, R. S., Perring, A. E., Cross, E., Onasch, T. B., Ahern, A., Wrobel, W., Davidovits, P., Olfert, J., Dubey, M. K., Mazzoleni, C., and Fahey, D. W.: The detection efficiency of the single particle soot photometer, Aerosol Sci. Technol., 44, 612–628, https://doi.org/10.1080/02786826.2010.481298, 2010.

Sedlacek, A. J., Onasch, T. B., Nichman, L., Lewis, E. R., Davidovits, P., Freedman, A., and Williams, L.: Formation of refractory black carbon by SP2-induced charring of organic aerosol, Aerosol Sci. Technol., 52, 1521–7388, https://doi.org/10.1080/02786826.2018.1531107, 2018.

Sharma, S., Leaitch, W. R., Huang, L., Veber, D., Kolonjari, F., Zhang, W., Hanna, S. J., Bertram, A. K., and Ogren, J. A.: An evaluation of three methods for measuring black carbon in Alert, Canada, Atmos. Chem. Phys., 17, 15225–15243, https://doi.org/10.5194/acp-17-15225-2017, 2017.

Slowik, J. G., Cross, E. S., Han, J.-H., Davidovits, P., Onasch, T. B., Jayne, J. T., Williams, L. R., Canagaratna, M. R., Worsnop, D. R., Chakrabarty, R. K., Moosmüller, H., Arnott, W. P., Schwarz, J. P., Gao, R.-S., Fahey, D. W., Kok, G. L., and Petzold, A.: An inter-comparison of instruments measuring black carbon content of soot particles, Aerosol Sci. Technol., 41, 295–314, https://doi.org/10.1080/02786820701197078, 2007.

Sokolik, I. N. and Toon, O. B.: Incorporation of mineralogical composition into models of the radiative properties of mineral aerosol from UV to IR wavelengths, J. Geophys. Res.-Atmos., 104, 9423–9444, https://doi.org/10.1029/1998JD200048, 1999.

Spindler, G., Brüggemann, E., Gnauk, T., Grüner, A., Müller, K., and Herrmann, H.: A four-year size-segregated characterization study of particles PM_{10}, $PM_{2.5}$ and PM_1 depending on air mass origin at Melpitz, Atmos. Environ., 44, 164–173, https://doi.org/10.1016/j.atmosenv.2009.10.015, 2010.

Spindler, G., Gnauk, T., Gruener, A., Iinuma, Y., Mueller, K., Scheinhardt, S., and Herrmann, H.: Size-segregated characterization of PM_{10} at the EMEP site Melpitz (Germany) using a five-stage impactor: A six year study, J. Atmos. Chem., 69, 127–157, https://doi.org/10.1007/s10874-012-9233-6, 2012.

Spindler, G., Grüner, A., Mueller, K., Schlimper, S., and Herrmann, H.: Long-term size-segregated particle (PM_{10}, $PM_{2.5}$, PM_1) characterization study at Melpitz - Influence of air mass inflow, weather conditions and season, J. Atmos. Chem., 70, 165–195, https://doi.org/10.1007/s10874-013-9263-8, 2013.

Stephens, M., Turner, N., and Sandberg, J.: Particle identification by laser-induced incandescence in a solid-state laser cavity, Appl. Opt., 42, 3726, https://doi.org/10.1364/AO.42.003726, 2003.

Subramanian, R., Khlystov, A. Y., and Robinson, A. L.: Effect of peak inert-mode temperature on elemental carbon measured using thermal-optical analysis, Aerosol Sci. Technol., 40, 763–780, https://doi.org/10.1080/02786820600714403, 2006.

Tirpitz, J.-L., Frieß, U., Hendrick, F., Alberti, C., Allaart, M., Apituley, A., Bais, A., Beirle, S., Berkhout, S., Bognar, K., Bösch, T., Bruchkouski, I., Cede, A., Chan, K. L., den Hoed, M., Donner, S., Drosoglou, T., Fayt, C., Friedrich, M. M., Frumau, A., Gast, L., Gielen, C., Gomez-Martín, L., Hao, N., Hensen, A., Henzing, B., Hermans, C., Jin, J., Kreher, K., Kuhn, J., Lampel, J., Li, A., Liu, C., Liu, H., Ma, J., Merlaud, A., Peters, E., Pinardi, G., Piters, A., Platt, U., Puentedura, O., Richter, A., Schmitt, S., Spinei, E., Stein Zweers, D., Strong, K., Swart, D., Tack, F., Tiefengraber, M., van der Hoff, R., van Roozendael, M., Vlemmix, T., Vonk, J., Wagner, T., Wang, Y., Wang, Z., Wenig, M., Wiegner, M., Wittrock, F., Xie, P., Xing, C., Xu, J., Yela, M., Zhang, C., and Zhao, X.: Intercomparison of MAX-DOAS vertical profile retrieval algorithms: studies on field data from the CINDI-2 campaign, Atmos. Meas. Tech., 14, 1–35, https://doi.org/10.5194/amt-14-1-2021, 2021.

van Pinxteren, D., Mothes, F., Spindler, G., Fomba, K. W., and Herrmann, H.: Trans-boundary PM10: Quantifying impact and sources during winter 2016/17 in eastern Germany, Atmos. Environ., 200, 119–130, https://doi.org/10.1016/j.atmosenv.2018.11.061, 2019.

Vecchi, R., Bernardoni, V., Fermo, P., Lucarelli, F., Mazzei, F., Nava, S., Prati, P., Piazzalunga, A., and Valli, G.: 4-hours resolution data to study PM10 in a "hot spot" area in Europe, Environ. Monit. Assess., 154, 283–300, https://doi.org/10.1007/s10661-008-0396-1, 2009.

Virkkula, A., Mäkelä, T., Hillamo, R., Yli-Tuomi, T., Hirsikko, A., Hämeri, K., and Koponen, I. K.: A simple procedure for correcting loading effects of aethalometer data, J. Air Waste Manag. Assoc., 57, 1214–1222, https://doi.org/10.3155/1047-3289.57.10.1214, 2007.

Wang, Y., Chung, A., and Paulson, S. E.: The effect of metal salts on quantification of elemental and organic carbon in diesel exhaust particles using thermal-optical evolved gas analysis, Atmos. Chem. Phys., 10, 11447–11457, https://doi.org/10.5194/acp-10-11447-2010, 2010.

Watson, J. G., Chow, J. C., and Chen, L.-W. A.: Summary of organic and elemental carbon/black carbon analysis methods and intercomparisons, Aerosol Air Qual. Res., 5, 65–102, https://doi.org/10.4209/aaqr.2005.06.0006, 2005.

Wehner, B., Philippin, S., Wiedensohler, A., Scheer, V., and Vogt, R.: Variability of non-volatile fractions of atmospheric aerosol particles with traffic influence, Atmos. Environ., 38, 6081–6090, https://doi.org/10.1016/j.atmosenv.2004.08.015, 2004.

Weingartner, E., Saathoff, H., Schnaiter, M., Streit, N., Bitnar, B., and Baltensperger, U.: Absorption of light by soot particles: determination of the absorption coefficient by means of aethalometers, J. Aerosol Sci., 34, 1445–1463, https://doi.org/10.1016/S0021-8502(03)00359-8, 2003.

Wiedensohler, A., Birmili, W., Nowak, A., Sonntag, A., Weinhold, K., Merkel, M., Wehner, B., Tuch, T., Pfeifer, S., Fiebig, M., Fjäraa, A. M., Asmi, E., Sellegri, K., Depuy, R., Venzac, H., Villani, P., Laj, P., Aalto, P., Ogren, J. A., Swietlicki, E., Williams, P., Roldin, P., Quincey, P., Hüglin, C., Fierz-Schmidhauser, R., Gysel, M., Weingartner, E., Riccobono, F., Santos, S., Grüning, C., Faloon, K., Beddows, D., Harrison, R., Monahan, C., Jennings, S. G., O'Dowd, C. D., Marinoni, A., Horn, H.-G., Keck, L., Jiang, J., Scheckman, J., McMurry, P. H., Deng, Z., Zhao, C. S., Moerman, M., Henzing, B., de Leeuw, G., Löschau, G., and Bastian, S.: Mobility particle size spectrometers: harmonization of technical standards and data structure to facilitate high quality long-term observations of atmospheric particle number size distributions, Atmos. Meas. Tech., 5, 657–685, https://doi.org/10.5194/amt-5-657-2012, 2012.

WMO: WMO-No. 1177, GAW Report No. 227, available at: https://library.wmo.int/doc_num.php?explnum_id=3073 (last access: 16 February 2021), WMO/GAW Aerosol Measurement Procedures, Guidelines and Recommendations, World Meteorological Organization, Geneva, Switzerland, 93 pp., 2nd Edn., 2016.

Yu, J. Z., Xu, J., and Yang, H.: Charring characteristics of atmospheric organic particulate matter in thermal analysis, Environ. Sci. Technol., 36, 754–761, https://doi.org/10.1021/es015540q, 2002.

Yuan, J., Modini, R. L., Zanatta, M., Herber, A. B., Müller, T., Wehner, B., Poulain, L., Tuch, T., Baltensperger, U., and Gysel-Beer, M.: Variability in the mass absorption cross section of black carbon (BC) aerosols is driven by BC internal mixing state at a central European background site (Melpitz, Germany) in winter, Atmos. Chem. Phys., 21, 635–655, https://doi.org/10.5194/acp-21-635-2021, 2021.

Zhang, X., Kim, H., Parworth, C. L., Young, D. E., Zhang, Q., Metcalf, A. R., and Cappa, C. D.: Optical properties of wintertime aerosols from residential wood burning in Fresno, CA: results from DISCOVER-AQ 2013, Environ. Sci. Technol., 50, 1681–1690, https://doi.org/10.1021/acs.est.5b04134, 2016.

Zhang, Y., Favez, O., Canonaco, F., Liu, D., Močnik, G., Amodeo, T., Sciare, J., Prévôt, A. S. H., Gros, V., and Albinet, A.: Evidence of major secondary organic aerosol contribution to lensing effect black carbon absorption enhancement, NPJ Clim. Atmos. Sci., 1, 47, https://doi.org/10.1038/s41612-018-0056-2, 2018.

Zhang, Y. L., Perron, N., Ciobanu, V. G., Zotter, P., Minguillón, M. C., Wacker, L., Prévôt, A. S. H., Baltensperger, U., and Szidat, S.: On the isolation of OC and EC and the optimal strategy of radiocarbon-based source apportionment of carbonaceous aerosols, Atmos. Chem. Phys., 12, 10841–10856, https://doi.org/10.5194/acp-12-10841-2012, 2012.

Zhu, Y., Kuhn, T., Mayo, P., and Hinds, W. C.: Comparison of daytime and nighttime concentration profiles and size distributions of ultrafine particles near a major highway, Environ. Sci. Technol., 40, 2531–2536, https://doi.org/10.1021/es0516514, 2006.

Zotter, P., Herich, H., Gysel, M., El-Haddad, I., Zhang, Y., Močnik, G., Hüglin, C., Baltensperger, U., Szidat, S., and Prévôt, A. S. H.: Evaluation of the absorption Ångström exponents for traffic and wood burning in the Aethalometer-based source apportionment using radiocarbon measurements of ambient aerosol, Atmos. Chem. Phys., 17, 4229–4249, https://doi.org/10.5194/acp-17-4229-2017, 2017.